

Course AE4133

CFD II Part 2: Computation and Modelling of Turbulence

April 2015 (Version 2015.2)

Faculty of
Aerospace Engineering

S.J. Hulshoff

HSL 0.36, Aerodynamics Group
S.J.Hulshoff@TUDelft.NL



Artikelnummer 06917730033

Contents

1	Introduction	5
1.1	Overview	5
1.2	The Definition of Turbulence	5
1.3	The Analysis of Turbulence	6
1.4	The Modelling of Turbulence	7
1.5	The Computation of Turbulence	8
1.6	An Outline of CFD II, Part 2	9
2	Physics of Turbulent flows	11
2.1	The Energy Cascade	11
2.1.1	The necessity for three dimensions	14
2.2	Isotropic turbulent flows	16
2.3	Wall-bounded turbulent flows	16
2.3.1	Wall units	17
2.3.2	Mean-flow topology	17
2.3.3	Coherent structures	20
2.3.4	Size of the Kolmogorov scales	21
3	Direct Numerical Simulation	23
3.1	The cost of DNS	23
3.2	Numerical Methods for DNS	24
3.2.1	Spectral Methods	24
3.2.2	Finite-Difference and Finite-Element Methods	24
3.2.3	Boundary conditions	25
3.3	DNS Example: Channel flow	26
4	Large-Eddy Simulation	31
4.1	Scale separation using filtering	31
4.2	The Filtered Navier-Stokes Equations	32
4.3	The Resolved kinetic energy equation	33
4.4	The Smagorinsky model	34
4.4.1	Calibration of the Smagorinsky model	35
4.5	Dynamic Modelling	35
4.6	Modern SGS models	37

4.7	Some example results	38
4.8	LES of wall-bounded flows	38
4.9	Subtle Issues with Filter-Based Techniques	41
4.10	The Multiscale Approach to LES	42
4.10.1	Analysis of a general problem	42
4.10.2	Approximation of u' for linear advection	44
4.10.3	An implementation for LES	47
4.10.4	A three-scale VMM	49
5	RANS Methods	59
5.1	Reynolds-averaged Navier-Stokes equations	59
5.2	Additional dynamic relations	61
5.2.1	The Reynolds-stress equations	61
5.2.2	The turbulent kinetic energy equation	62
5.3	Linear eddy-viscosity models (LEVM)	62
5.3.1	An example LEVM: The Spalart-Allmaras model	63
5.3.2	Limitations of LEVM	66
5.4	Non-linear constitutive relations (NLCR)	68
5.4.1	Non-linear eddy viscosity models (NLEVM)	69
5.4.2	Algebraic Reynolds stress models (ARSM)	70
5.4.3	Limitations of NLCR models	71
5.5	Reynolds-stress transport (RST) models	71
5.5.1	Modelling of redistribution terms	71
5.5.2	Modelling of pressure-strain terms	72
5.5.3	Modelling of the dissipation rate tensor	72
5.5.4	RST models in practice	73
5.6	Wall functions	73
6	Hybrid Methods	75
6.1	RANS, LES, URANS and Hybrids	75
6.2	Detached Eddy Simulation (DES)	76
A	The Navier-Stokes equations	85
A.1	The incompressible Navier-Stokes Equations (NSE)	85
A.2	The equation for pressure	85
A.3	The equation for vorticity	86

Chapter 1

Introduction

1.1 Overview

These notes provide an overview of computational methods for turbulence, and in particular methods for the computation of wall-bounded turbulent flows. They review the most pertinent physical phenomena, and describe and contrast the techniques currently used for numerical simulation.

In the following introduction, we begin by briefly describing the properties of turbulent flows, and the main theoretical approaches which have been used to analyse them. Then a short history of numerical techniques for predicting turbulence is given. The details of these techniques will be described in the remainder of the notes.

1.2 The Definition of Turbulence

Most references define turbulence indirectly, in terms of observed properties. The following are based on those described in [73]:

1. **Turbulence has intrinsic spatial and temporal complexity** At high Reynolds numbers, flows described by the Navier-Stokes equations exhibit extreme sensitivity to disturbances. Turbulence is the chaotic response to such disturbances, with a complexity so high that its behaviour is often considered to be stochastic. In this sense it is self-stochastic, as it can maintain its complex state in the absence of new disturbances or external forcing.
2. **Turbulence is three-dimensional and rotational** Three-dimensional turbulent flows self-amplify the velocity derivatives of their larger scales. This results in a continuous net production of strain, $s_{ij} = (\partial u_i / \partial x_j + \partial u_j / \partial x_i) / 2$ and enstrophy, $|\omega|^2$, where vorticity $\omega = \nabla \times \mathbf{u}$. The enstrophy is dissipated at smaller scales by viscosity and the strain field.

3. **Turbulence has a wide range of strongly-interacting scales** The non-linear convection term in the Navier-Stokes equations leads to strong interactions between different length scales. The range of scales involved is normally wide, and increases with Reynolds number. For flows around aircraft, for example, a typical range is from several metres to less than a micrometre ($\sim 10^{22}$ spectral degrees of freedom).
4. **Turbulence is highly dissipative** The turbulent kinetic energy generated within a flow is ultimately dissipated by viscosity at its smallest scales. Turbulent flows require a significant source of energy to maintain them. They are statistically irreversible, and are thus one way in time.
5. **Turbulence is highly diffusive** Turbulent flows have strongly enhanced transport of momentum, energy and passive scalars (i.e. weightless particles). This property is not unique to turbulence, however, as random velocity fields and Lagrangian-chaotic laminar flows can also have enhanced transport of passive scalars .
6. **Turbulence is statistically stable** The details of turbulent flows with identical boundary conditions can change dramatically from one realisation to another. It has been observed, however, that their statistical properties remain the same.

Due to the complexity of turbulent flows, much of the knowledge about their characteristics has been generated experimentally. When they are studied theoretically or computationally, the Navier-Stokes equations (NSE) are normally used. It is possible that this is not always appropriate, as there might be local high-gradient areas in turbulent flows where the Newtonian or continuum assumptions break down. Comparisons of theoretical and computational NSE results with experimental data, however, seems to confirm that the NSE describe all of the important dynamics of turbulence encountered in typical engineering applications.

1.3 The Analysis of Turbulence

The analysis of turbulence has essentially followed three parallel movements: statistical, structural, and deterministic [43, 9]. Initially, the *statistical* viewpoint put forth by Reynolds in the 1890's prevailed. This implied that there was little practical information to be gained by studying the complex details of turbulent flows, so efforts should instead be made to characterise their statistical behaviour. This view was dominant until mid-way through the twentieth century, and has led to extensive theoretical results.

In the 1950's, however, experimental wall-bounded turbulent-flow data began to appear which showed velocities at different spatial and temporal positions to be highly correlated [7]. This led to the conclusion that coherent structures must exist in turbulent flows, and therefore they could not be completely random. The result was the birth of the *structural* movement. Since that time,

using both experimental and numerical observations, rich phenomenological descriptions have been built for certain classes of turbulent flows. These descriptions are useful both for modelling turbulence and attempting to control its behaviour.

In 1963 Lorenz [39] presented a numerical solution for a model of the Navier-Stokes equations which reproduced some of the crucial aspects of turbulent flows, including extreme sensitivity to initial conditions and responses complex enough to appear random. This can be seen as the start of the *deterministic* movement, which views turbulence as a complex and chaotic solution of the Navier-Stokes equations. In 1972, the first numerical simulations of turbulent flows were performed by Orszag and Patterson [49]. These demonstrated how deterministic ideas could be used to produce useful results.

In the next section three approaches to computing turbulent flows will be discussed. The first of these, based on the use of the Reynolds-averaged equations, is primarily statistical in nature. The other two, direct numerical and large-eddy simulation, are rooted in the deterministic viewpoint.

1.4 The Modelling of Turbulence

In 1895 Reynolds suggested the decomposition of the velocity field into mean and fluctuating parts as a first step towards the representation of turbulent flows. This idea was based on the observation that many turbulent flows have reproducible averages, and it is their averages rather than their fluctuations which are normally of practical interest. The Reynolds decomposition leads to equations for the mean velocities and pressure, known as the Reynolds-averaged Navier-Stokes equations (RANS). These include terms containing the unknown fluctuations. In order to complete the system, a model which defines the effect of the fluctuations on the mean is required. Such models are referred to as turbulence models, as in essence they must represent all the effects of turbulence within the flow. They reflect a statistical viewpoint, as they do not employ a detailed computation of turbulence dynamics, but instead try to reproduce the global effects of turbulence on the mean using theoretical and empirical input.

The development of turbulence models has received much attention over the last century, with notable examples including the early mixing length model developed by Prandtl (1925), the $k - \epsilon$ model developed by Launder (1972), and the now popular Spalart-Almaras (1992) and Menter SST (1994) models. Reviews covering the subject of modelling, and in particular its application to aerospace engineering, include [16, 57] and [33]. The level of modelling sophistication in RANS can be very high, normally requiring the solution of one or more additional non-linear partial differential equations. In spite of this, significant model calibration is required, and even the most advanced turbulence models still suffer from a lack of generality. In particular, RANS models are unable to predict flows with smooth separation accurately, and are limited in their ability to predict transition.

1.5 The Computation of Turbulence

A strict interpretation of the deterministic viewpoint requires the full computation of all turbulence dynamics within a flow, for a period long enough to ensure the reliable determination of statistics. This approach, known as direct numerical simulation (DNS) is only possible for Reynolds numbers in the low thousands. As the Reynolds number is increased, the range of scales which must be resolved increases, and the computing power required increases enormously (roughly with the cube of the Reynolds number). Reynolds numbers which are of interest for engineering will likely remain intractable for several decades to come. DNS has played an essential role in the development of the understanding of turbulence, however, by providing detailed and precise descriptions of low Reynolds number phenomena.

A far more viable deterministic option is large-eddy simulation (LES). In LES, the dynamics of the largest eddies are computed (resolved), while models are used to represent the effects of the non-computed (unresolved) scales. This approach is motivated by the fact that it is the largest scales which are normally of interest in engineering applications. It is also the largest scales which are the most affected by the geometry and boundary conditions of a problem. In contrast, the smaller scales tend to interact more locally, and are thus more amenable to modelling. Models for the small scales may be developed from a statistical viewpoint, but the overall approach of LES is deterministic, as mean flow properties are obtained through long-time simulations of large-scale turbulence dynamics. As only part of the scale range needs to be simulated, LES is becoming more and more practical for many applications. In order to perform reliable LES of wall-bounded flows, however, special care must be taken in unresolved-scale modelling due to the anisotropic behaviour of turbulent flows in the vicinity of a wall. General reviews of LES techniques can be found in [58, 50].

In order to provide a precise definition of the resolved and unresolved scales in LES, the concept of filtering is often used. When this is done explicitly, by choosing a filter width much larger than the mesh spacing, it is possible to separate errors in the modelling of the unresolved scales from discretisation errors. In practice, however, it is more practical to set the filter width close to the mesh size, or interpret the mesh itself as a filter. As a result there is often a strong interaction between model and discretisation errors. This interaction is taken into account in the design of advanced LES techniques. An alternative to the filtering concept is to use the variational multiscale method [24], in which discretisation error and model error are unified and described by a separate evolution equation. This simplifies the analysis somewhat, particularly near domain boundaries where the filtering concept requires special treatment.

1.6 An Outline of CFD II, Part 2

In the remainder of these notes the basic processes of turbulence will first be discussed, including phenomenological behaviours and scaling characteristics. Then methods for direct numerical simulation will be described and some key results examined. After that, methods for large-eddy simulation will be reviewed, including both filtered-based and variational-multiscale approaches. Finally the RANS approach will be described, and the design and limitations of the most popular RANS turbulence models discussed.

Chapter 2

Physics of Turbulent flows

In this chapter we review some physical characteristics of turbulent flow which directly affect the design of methods for predicting them. These reflect only a subset of the theory and observations which have appeared over the last century. For a more complete overview, the reader is referred to general textbooks on the subject including [73, 7, 43].

2.1 The Energy Cascade

In the analysis of turbulent flows it is normal to speak of an energy cascade, a process where the kinetic energy of larger eddies is (on average) transferred to slightly smaller eddies. This process is inherently three dimensional, and is often described in terms of vortex stretching and tilting, or alternatively in terms of helical pairing interactions. Although some energy dissipation occurs at all scales, the large scales are primarily inviscid, and the majority of their kinetic energy is transferred down through the cascade to the smallest, viscous-dominated scales where it is finally dissipated and converted to heat. The separation between the largest and smallest scales is thus directly determined by relative viscosity. As the Reynolds number is increased, the ratio of the largest to the smallest scales is also increased.

It is normal to visualise the energy distribution across scales using the turbulent kinetic energy spectrum. To define the spectrum, we consider a decomposition of the total velocity into a mean component \bar{u}_i , and a fluctuating component u'_i . The turbulent kinetic energy is then defined as:

$$k = \frac{1}{2} u'_i u'_i \quad (2.1)$$

Introducing the wavenumber κ , we define the energy spectrum, $E(\kappa)$, such that

$$k = \int_0^\infty E(\kappa) d\kappa \quad (2.2)$$

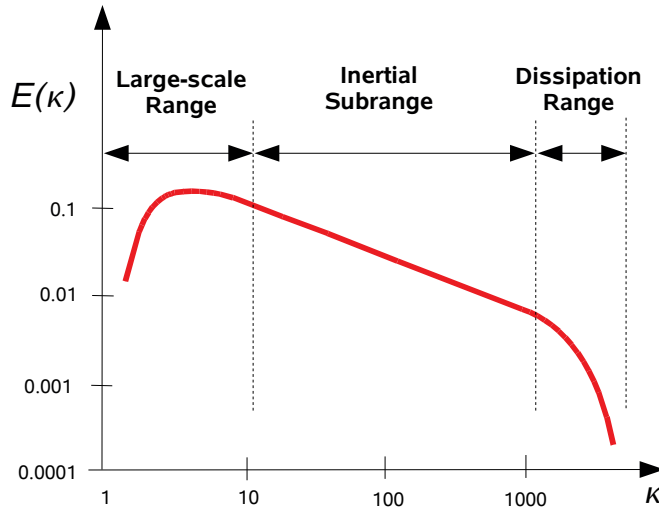


Figure 2.1: Energy spectrum for a turbulent flow

which implies that the kinetic energy of eddies between the wave numbers κ and $\kappa + d\kappa$ is

$$E(\kappa) d\kappa \quad (2.3)$$

A typical plot of $E(\kappa)$ for a turbulent flow is given in figure 2.1 (note that the wavenumber is proportional to the inverse of the eddy length scales).

In the 1940's, Kolmogorov [32, 31] developed the universal equilibrium theory to describe the behaviour of turbulent flows. In it he invoked the concept of scale separation, by assuming that the dynamics of the smallest scales are statistically independent of those of the largest scales. Correspondingly, the behaviour of the smallest scales is only determined by the energy transferred to them from the largest scales via the cascade, and by the effects of kinematic viscosity. If the turbulent flow is in equilibrium, the rate of energy supplied from the largest turbulent scales will balance the rate of energy dissipation of the smallest scales. Kolmogorov also postulated the existence of an intermediate range of scales which is independent of the dynamics of both the large and small scales. It is thus natural to divide figure 2.1 into three regions, as described below.

1. **Large-scale range** The largest scales in the flow are those responsible for turbulence production, and carry the majority of turbulent kinetic energy. They extract kinetic energy from the mean flow, and have comparable length and velocity scales. They are thus subject to the macroscopic effects of geometry and forcing, and are of primary importance in the determination of the forces and moments which are of most interest to the engineer.
2. **Inertial subrange** If the Reynolds number is sufficiently high, an inter-

mediate range of scales will exist which transfer the energy received from the large scales down the cascade, but in which negligible dissipation occurs. In this case it may be assumed that the local velocities only scale with the rate of energy transfer of energy from the large scales, ε and the local length scale, κ^{-1} . If so, we can write

$$E(\kappa) \sim \varepsilon^a (\kappa^{-1})^b \quad (2.4)$$

$$\left[\frac{m^3}{s^2} \right] \sim \left[\frac{m^2}{s^3} \right]^a [m]^b \quad (2.5)$$

which results in two simultaneous equations, $2a + b = 3$ and $a = 2/3$. Thus in the inertial subrange:

$$E(\kappa) \sim \varepsilon^{\frac{2}{3}} \kappa^{-\frac{5}{3}} \quad (2.6)$$

$$(2.7)$$

or

$$E(\kappa) = C_K \varepsilon^{\frac{2}{3}} \kappa^{-\frac{5}{3}} \quad (2.8)$$

where C_K is the Kolmogorov constant. The variation of the inertial subrange of the spectrum with $\kappa^{-\frac{5}{3}}$ has been observed experimentally in a wide range of turbulent flows, with typical values for C_K found to be near 1.4.

- 3. Dissipation range** In the dissipation range, the behaviour of eddies is assumed to be dominated by the viscosity, ν and the rate of energy transferred from the large scales ε . Characteristic length, time and velocity scales can again be derived using dimensional analysis. An expression for the smallest relevant length scale, η , can be obtained from the viscosity, ν and the energy dissipation rate, ε by writing:

$$\eta \sim \nu^a \varepsilon^b \quad (2.9)$$

$$[m] \sim \left[\frac{m^2}{s} \right]^a \left[\frac{m^2}{s^3} \right]^b \quad (2.10)$$

Which leads to the two simultaneous equations, $1 = 2a + 2b$ and $0 = -a - 3b$. Solving for a and b gives the expression for the Kolmogorov length scale:

$$\eta \sim \left(\frac{\nu^3}{\varepsilon} \right)^{1/4} \quad (2.11)$$

Similarly, expressions for the Kolmogorov time and velocity scales can be derived:

$$\tau \sim \left(\frac{\nu}{\varepsilon} \right)^{1/2} \quad (2.12)$$

$$v \sim (\nu \varepsilon)^{1/4} \quad (2.13)$$

Since the scales of the dissipation range are assumed to be independent of the largest scales of the flow, they have no awareness of geometric boundaries. Correspondingly, they are normally assumed to be isotropic.

Kolmogorov's description is very useful conceptually, and also predicts the correct order of turbulent scales. It should be kept in mind, however, that it remains an idealisation. The real behaviour of turbulent flows can be considerably more intricate. It has been shown, for example, that dissipation does not actually occur uniformly in space, but tends to be concentrated in relatively compact regions [7]. It is also incorrect to visualise energy transfer in the cascade as uni-directional (i.e. only from large to small). Local interactions between like scales can transfer kinetic energy in both directions. It is only the average transfer of kinetic energy which is from large to small scales.

2.1.1 The necessity for three dimensions

In three-dimensional flows, there exists a number of mechanisms for transferring energy between scales. For turbulent 3D flows a prominent mechanism is vortex stretching, which transfers kinetic energy from larger to smaller scales. Consider the equation for vorticity, derived from the incompressible Navier-Stokes equations in appendix A.3:

$$\frac{\partial \boldsymbol{\omega}}{\partial t} + \mathbf{u} \cdot \nabla \boldsymbol{\omega} = \mathbf{S} \cdot \boldsymbol{\omega} + \nu \nabla^2 \boldsymbol{\omega} \quad (2.14)$$

This equation says that vorticity is modified both by the strain rate and viscous effects as it is advected through the flow. In figure 2.2, a patch of vorticity passes through a contraction. The flow accelerates, so $S_{11} = \partial u / \partial x$ is positive. To satisfy continuity, S_{22} and S_{33} are therefore negative. Ignoring viscous effects, ω_1 is thus amplified, while ω_2 and ω_3 decay. This can be seen as a direct consequence of the conservation of angular momentum. If a rotating fluid element is reduced in scale relative to its axis of rotation, its angular velocity must increase.

A free straight-line vortex will not cause itself to stretch, but in a turbulent flow there are many neighbouring vortices which can induce stretching velocity fields. If through stretching, increased velocity gradients occur on a scale small enough to incur significant viscous dissipation, then kinetic energy will be removed from the flow, making its transfer one-sided.

Note that the stretching mechanism simply does not occur in two-dimensional flows. In two dimensions, all velocity gradients are in plane, while the vorticity vector is directed out of plane. Therefore $\mathbf{S} \cdot \boldsymbol{\omega} = 0$. As a consequence, two-dimensional vortical flows behave quite differently. Firstly, isolated 2D patches of vorticity are most stable when they are circular. Isolated non-circular patches of vorticity will induce a velocity field on themselves which tends to drive them towards a circular geometry. Secondly, when two 2D patches of vorticity become sufficiently close to each other, they have a tendency to merge.

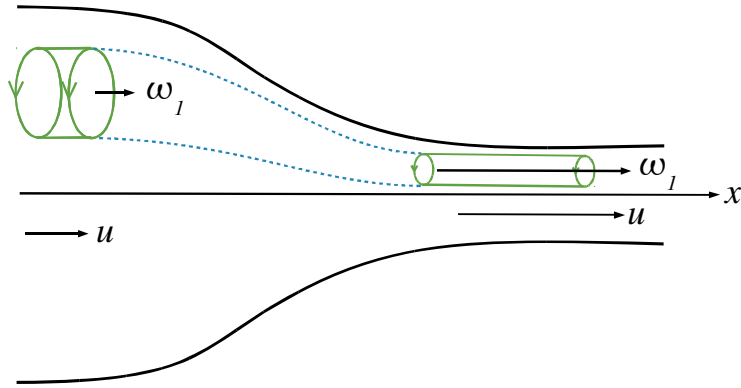


Figure 2.2: Stretching of a vortex due to a contraction (after reference [72])

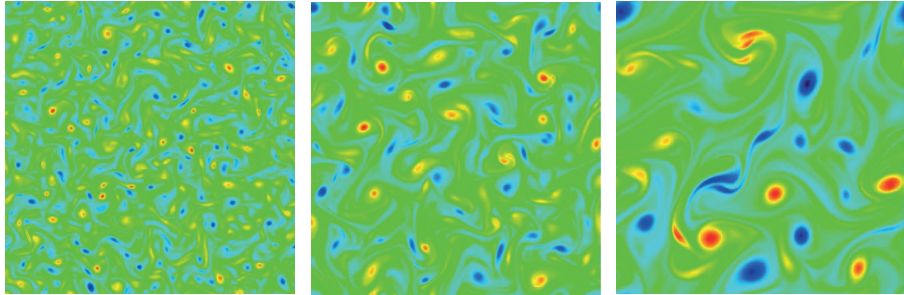


Figure 2.3: Evolution of a vorticity distribution in a two-dimensional periodic domain (Fluid Dynamics laboratory, TU Eindhoven)

Two-dimensional flows can still be “turbulent” in a sense, due to the occurrence of chaotic motion. The constraints of space and requirement for conservation of angular momentum means that two separated 2D vortices will interact in a fairly simple way. Once three or more vortices are present, however, their motion will become complex, and sensitive to initial conditions [27]. On the other hand because of vortex merging, 2D turbulent flows tend to transfer energy to larger and larger scales, and become more ordered in time. This is sometimes referred to as an inverse cascade process.

The fundamental differences between two and three-dimensional turbulence are summarised by the time histories shown figures 2.3 and 2.4. Clearly, two-dimensional simulations are not useful for predicting the behaviour of three-dimensional turbulence. Two-dimensional turbulence is relevant for weather prediction and oceanic research. It is encountered rarely, however, in engineering application. As the latter is the focus of our interest, from this point on the term turbulence will only be used to refer to three-dimensional turbulent flows.

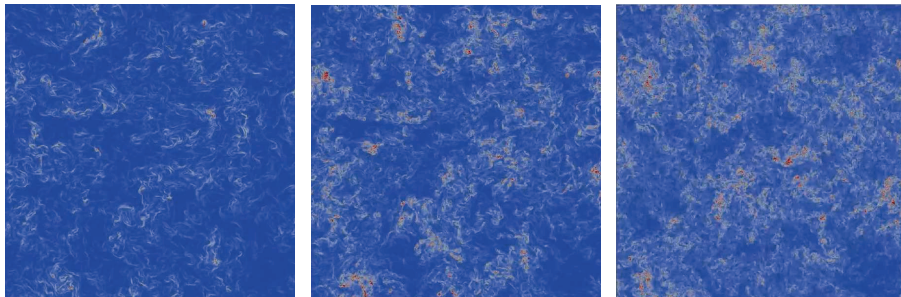


Figure 2.4: Evolution of energy dissipation in a three-dimensional periodic domain

2.2 Isotropic turbulent flows

Isotropic turbulent flows (those whose local statistics are independent of direction) are frequently referred to as they are convenient to treat mathematically, and are presumed to contain some basic turbulent physics which re-appear to one extent or another in all turbulent flows. In some sense they are the most “pure” as they are dominated by non-linear turbulent flow effects. The evolution shown in figure 2.4 is an example of an isotropic turbulent flow on a periodic domain.

Although useful from the theoretical standpoint, isotropic or quasi-isotropic flows are quite difficult to produce experimentally (and to some extent, numerically). Approximately isotropic flows can be made for experiments using grids and gratings. For computations, specialised initial conditions and forcing terms must be used. In view of our goal of computing wall-bounded flows, our interest in isotropic turbulent flows will be limited to their use in subgrid modelling, where isotropic assumptions are often invoked.

2.3 Wall-bounded turbulent flows

Wall-bounded flows may be broadly divided into two classes: external and internal. External wall-bounded turbulent flows are mixed in the sense that they coexist with laminar regions (figure 2.5). The interface between the two regions normally contains rapid variations between laminar and turbulent flow. In internal flows, such intermittent behaviour is much less pronounced. In spite of this, external and internal flows share some important characteristics. Even in the mean sense, wall-bounded flows are anisotropic, in that the length scales of turbulent structures decrease rapidly as the wall is approached. Near the wall, turbulent behaviour is strongly influenced by the wall’s presence. As a result, part of the near-wall behaviour of internal flows is similar to that of external flows.

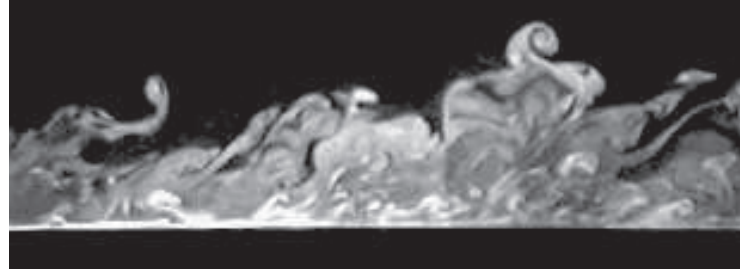


Figure 2.5: Laser-induced fluorescence image of an incompressible turbulent boundary layer, by C. Delo (Princeton)

2.3.1 Wall units

Based on the observation all wall-bounded flows contain similar features in the immediate vicinity of the wall, it makes sense to define a local system of non-dimensionalisation in which these features can be directly compared. This can be done by noting that in the immediate vicinity of a wall, velocities are low and viscous forces dominate. This leads to an estimate of scales which are indicative of the near-wall turbulent eddies. When used for the purpose of non-dimensionalisation, these scales are referred to as “wall units”.

If we consider wall-bounded flows for which mean streamwise gradients are relatively small, a viscous time scale can be defined in terms of the inverse of the mean wall vorticity as:

$$t_\nu = \left(\frac{\partial \bar{u}}{\partial y} \Big|_{y=0} \right)^{-1} \quad (2.15)$$

where \bar{u} is the mean streamwise velocity and y is the coordinate measured normal to the wall. We can also define a corresponding viscous length scale $l_\nu = \sqrt{\nu t_\nu}$. The so-called friction velocity then follows directly as:

$$u_\tau = \frac{l_\nu}{t_\nu} = \sqrt{\nu \frac{\partial \bar{u}}{\partial y} \Big|_{y=0}} = \sqrt{\frac{\tau_w}{\rho}} \quad (2.16)$$

These reference quantities allow local lengths and velocities to be expressed in terms of wall units as:

$$y^+ = y/l_\nu = y u_\tau / \nu \quad (2.17)$$

$$u^+ = u/u_\tau \quad (2.18)$$

2.3.2 Mean-flow topology

When discussing wall-bounded flows, it is normal to divide them into several different layers, as shown in figure 2.6. As can be anticipated, in the inner

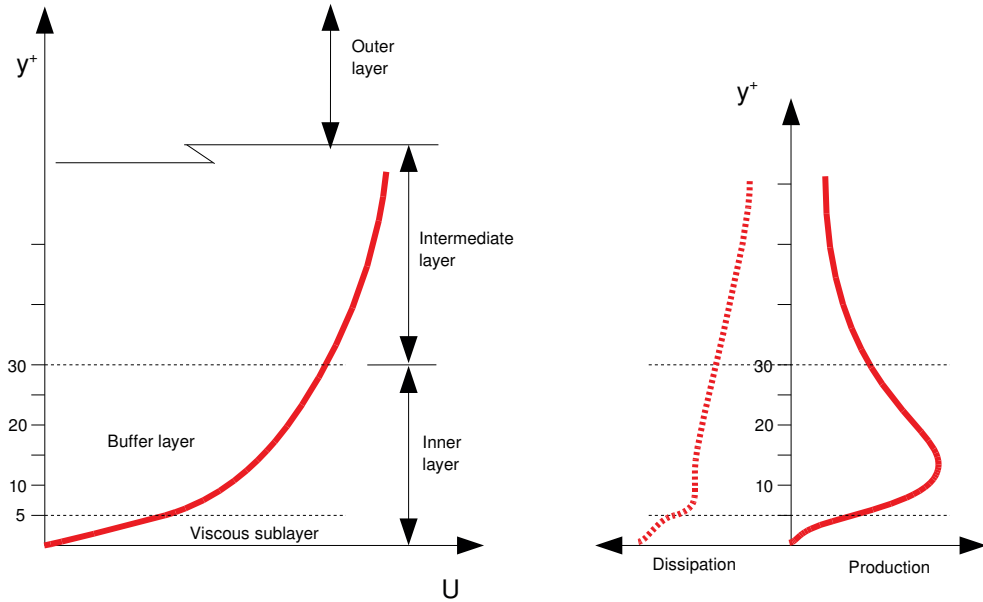


Figure 2.6: Nomenclature for wall-bounded turbulent flows (left) and typical turbulent energy production and dissipation curves

layer viscosity contributes significantly to the flow behaviour. It is itself divided into the viscous sublayer, where viscous effects dominate, and the buffer layer, where both viscous and vortical phenomena are important, and where much of the turbulence production takes place.

In the intermediate layer, viscous stresses are unimportant, and the flow is instead dominated by inviscid turbulent phenomena. Similarity laws, such as power laws or the log law, are normally used to describe this region. Finally there is the outer layer. In an external boundary layer these are regions with high intermittency, while in internal flows (such as pipe and channel flows) they have more regular perturbations.

The nomenclature for the layers can vary. The inner layer is sometimes referred to as the viscous or wall layer, and the intermediate layer as the overlap, fully turbulent, or log layer. The outer layer is also known as the wake region.

The near-wall velocity profile is often plotted using a semi-log plot, as shown in figure 2.7. By examining channel and pipe flows one can derive approximations for the mean velocity in the viscous sublayer and intermediate layers (see [7]). In the viscous sublayer, it can be shown that the mean velocity in terms of plus units, \bar{u}^+ , is given by:

$$\bar{u}^+ = y^+ \quad (2.19)$$

which is accurate for most wall-bounded flows until the limit of the viscous sublayer near $y^+ = 5$. In the intermediate layer, dimensional reasoning can also

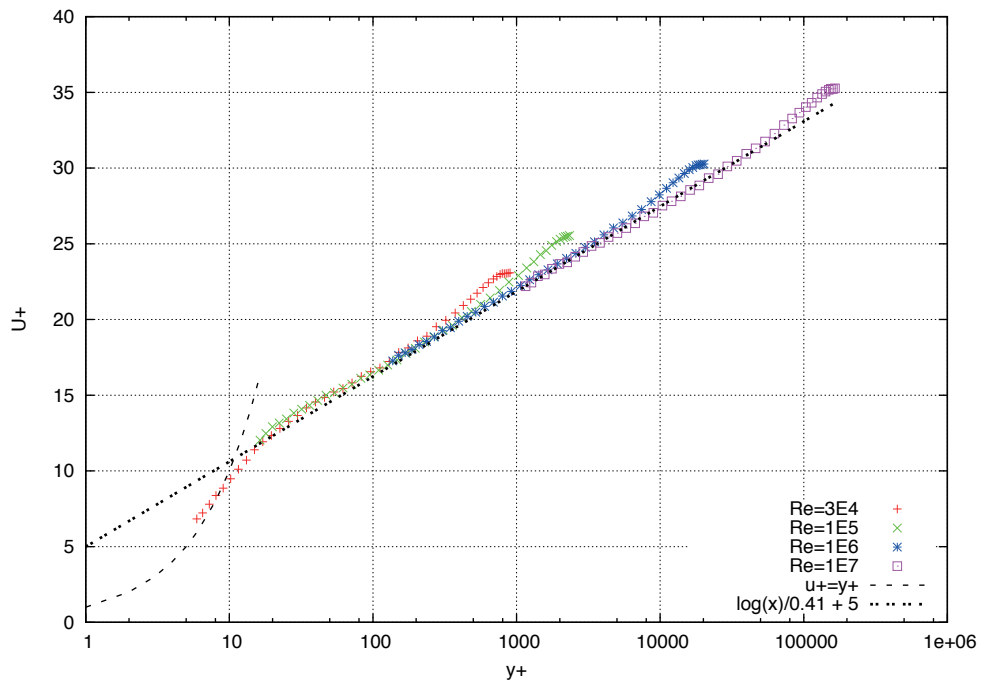


Figure 2.7: Experimental turbulent pipe flow velocity profiles for different Reynolds numbers plotted with viscous sublayer and log-law approximations (experimental data from [79]).



Figure 2.8: Appearance of near-wall streaks and generation of a turbulent spot during the transition process (KTH)

be used to arrive at the conclusion that

$$\bar{u}^+ = f(y^+) \quad (2.20)$$

which is normally referred to as the law of the wall. A popular law of the wall is the log law:

$$\bar{u}^+ = \frac{1}{\kappa} \ln y^+ + B \quad (2.21)$$

where experimental values for the Karman constant, κ are near 0.4 while those for B range from 5 – 5.5. In the outer layer, experimental measurements suggest the use of velocity-defect laws, which have the form

$$\bar{u}^+ = \bar{u}_c^+ - g(y/R) \quad (2.22)$$

where in the case of pipe flow \bar{u}_c^+ is the mean centreline velocity and R is the pipe radius.

2.3.3 Coherent structures

A noticeable feature of wall bounded-flows is the appearance of low-speed streaks in the immediate vicinity of the wall (figure 2.8). These are typically spaced about 100 wall units apart, and have lengths of up to 1000 wall units. They reside normally near $y^+ = 5$, but can “lift up” from the wall and oscillate in the buffer layer $8 \leq y^+ \leq 12$, until participating in a “bursting” process in the region $10 \leq y^+ \leq 30$ (figure 2.9). The streaks are associated with streamwise vorticity, which is sometimes visualised as forming part of a hairpin vortex responsible for the lift-up process. Simultaneously, there is a reciprocal sweep of high-speed fluid towards the viscous sublayer. The bursting process is associated with the majority of the turbulent kinetic energy production from the wall to $y^+ = 100$ [7]. Its relatively compact extent imposes high resolution requirements on computations which are intended to capture the production of turbulence.

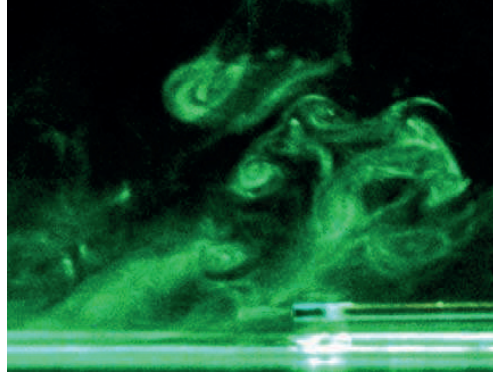


Figure 2.9: Vortex packet in a turbulent boundary layer (Center for Fluid Physics, University of New Hampshire)

The success of relations such as 2.21 implies some sort of universality of the near-wall flow when expressed in terms of wall units. Although this may be the case for quantities such as mean velocity, it has been demonstrated that average fluctuations expressed in wall units do vary with Reynolds number [26, 23]. Recent work indicates that examining the relations of the inner coherent structures with very large outer structures may provide models for these variations [42, 2].

2.3.4 Size of the Kolmogorov scales

An estimate of the size of the Kolmogorov scales can be used to test the validity of the continuum assumption, and to estimate the resolution required for direct numerical simulations. For wall-bounded flows, for example, the Kolmogorov scale has been found experimentally to be:

$$\eta^+ \equiv \eta u_\tau / \nu \approx (\kappa y^+)^{1/4} \quad (2.23)$$

where κ , the von Karman constant, has a value of approximately 0.4. The validity of the Navier-Stokes equations relies on the molecular mean free path, \mathcal{L} being much smaller than the Kolmogorov scale. Their ratio is called the turbulence Knudsen number, which can be expressed as [12]:

$$\text{Kn} = \frac{\mathcal{L}}{\eta} \approx \frac{Ma^{1/4}}{Re} \quad (2.24)$$

In practice, the high Mach number low Reynolds number combination which leads to violation of the continuum assumption is unusual.

In order to estimate sizes of the Kolmogorov scales as a function of Reynolds number, we employ the concept of the energy cascade, and assume the flow to be

in equilibrium. The largest turbulent eddies in the vicinity of the wall are still approximately inviscid, and have a kinetic energy proportional to the square of their characteristic velocity, u_l . The rate of transfer of energy is assumed to be proportional to the large eddy turn-over time, $t_l = l_l/u_l$, where l_l is the characteristic length of the largest eddies. Since kinetic energy is on average passed through the cascade to be dissipated by the smallest eddies in the flow, the rate of kinetic energy dissipation at the smallest scales can be estimated as:

$$\varepsilon \sim \frac{u_l^3}{l_l} \quad (2.25)$$

Using this estimate, the Kolmogorov scales can be determined with (2.11) – (2.13) to be:

$$\frac{\eta}{l_l} \sim \left(\frac{\nu}{u_l l_l} \right)^{3/4} = Re_l^{-3/4} \quad (2.26)$$

$$\frac{\tau u_l}{l_l} \sim \left(\frac{\nu}{u_l l_l} \right)^{1/2} = Re_l^{-1/2} \quad (2.27)$$

$$\frac{v}{u_l} \sim \left(\frac{\nu}{u_l l_l} \right)^{1/4} = Re_l^{-1/4} \quad (2.28)$$

These results are useful for estimating the scaling of numerical simulations with Reynolds number, as we will see in the next chapter.

Chapter 3

Direct Numerical Simulation

In a direct numerical simulation (DNS), all the relevant scales of motion are resolved. If one accepts that the Navier-Stokes equations are sufficient to model all aspects of turbulence, then direct numerical simulations of sufficient duration can provide precise statistics for turbulent flows. In practice, the cost of DNS can become prohibitive as the Reynolds number is increased. In spite of this, DNS is an extremely useful tool for research into turbulence phenomenology, and is frequently used to verify and calibrate less computing-intensive techniques such as LES and RANS. In this chapter we will examine some of the numerical aspects of DNS, and present some key results.

3.1 The cost of DNS

The high cost of direct numerical simulation limits the range of flows to which it can be applied. This can be appreciated by considering a model problem with a geometric (integral) length scale l_l . In order to simultaneously resolve phenomena with scale l_l and with the Kolmogorov length scale η , we would need at least l_l/η grid points in each direction. Since turbulent flow dynamics are inherently three-dimensional, the total number of grid points required, N , is proportional to $(l_l/\eta)^3$. From (2.26), we then have

$$N = N_x N_y N_z = O(Re_l^{9/4}) \quad (3.1)$$

In order to compute the unsteady dynamics of the Kolmogorov scales, the time step should be chosen such that $\Delta t = O(\eta/u_l)$, where u_l is the large-scale velocity. The simulation should also be run for several large-eddy turnover times, each of which has a length proportional to l_l/u_l . Therefore the number of required time steps, N_t , is also proportional to l_l/η , leading to a cost for DNS which scales with $(Re_l)^3$.

An example of a larger DNS simulation is that of Hoyas and Jimenez [23], who computed the flow in a turbulent channel at $Re_\tau = 2003$, or using the core velocity instead of u_τ , $Re_l \approx 40000$. This employed a mesh with dimension $N_x = 6144, N_y = 633, N_z = 4608$ and ran for 6×10^6 processor hours on 2048 processors (approximately 4 months of wall-clock time). A more recent example is that of Lee and Moser [35] who computed turbulent channel flow at $Re_\tau = 5200$ using $N_x = 10240, N_y = 1536, N_z = 7680$. This was run in a series of 524288-core jobs over a period of 9 months.

For aeronautical applications, we are interested in flows with $Re_l = O(10^7)$. Even if computing power can continue to increase at current rates, it will be several decades before we see DNS used for other than theoretical research or low Reynolds number applications.

3.2 Numerical Methods for DNS

DNS computations require algorithms with maximum efficiency. Therefore, emphasis has been placed on developing discretisations with a high accuracy per degree of freedom, efficient time-marching techniques and effective parallelisation. Correspondingly, the geometries considered tend to be simple ones, allowing maximum specialisation of the numerical method. This is not necessarily a disadvantage, as the even for simple geometries the information provided by DNS is rich and detailed, and not easy to interpret. For a general overview of the history of numerical methods in DNS, see [45].

3.2.1 Spectral Methods

The first techniques to be applied to DNS were spectral methods. These represent the solution in terms of global polynomials, which are normally chosen to be orthogonal for efficiency. Spectral methods can be shown to possess the property of exponential convergence, that is their truncation error decreases exponentially with the number of polynomials. When Fourier or Chebyshev modes are used for expansion, spectral methods can also be made relatively efficient using techniques such as the Fast Fourier Transform. Spectral methods were thus obvious choices for the first applications in DNS due to their margin of accuracy over finite-difference methods. They are highly suited to problems involving homogeneous turbulence, for which periodic boundary conditions are typically used. If non-periodic boundaries must be simulated, however, spectral methods become more complex to apply, particularly in parallel computing environments [36].

3.2.2 Finite-Difference and Finite-Element Methods

Finite difference and finite element methods differ primarily from spectral methods in the former are local. The finite element method in particular only differs from spectral methods in that the weight and interpolation functions are chosen

to have length scales related to the element size, rather than to the complete domain. This makes the application of boundary conditions far more straightforward, and facilitates partitioning based on geometric position for parallel computations.

Low-order finite-difference methods are particularly simple to implement but do not offer sufficient accuracy for application to DNS. The emphasis is thus on higher-order schemes. These can be constructed using increased stencils or via Padé schemes. In many applications, such as computational aeroacoustics, phase errors must be minimised, so that the design of the scheme for maximum order is bypassed in favour of reducing phase errors (e.g. [70]).

High-order finite-element methods also appear to be more effective than low-order ones. Their order is normally increased by adding functions to the interpolation of the solution within an element. This keeps the increases in degrees of freedom local to the element, which is convenient for parallel implementations, and offers the additional flexibility of being able to change the order locally in solution-adaptive methods. More recently it has been shown that the use of NURBS as basis functions, which allow the additional flexibility of refinement in function continuity (k -refinement) can be particularly effective [6].

3.2.3 Boundary conditions

To limit computational costs, it is normally desired to simulate only a portion of the physical domain. For flows which have homogeneous directions, this can be done by applying periodic conditions between boundaries placed far enough from each other so that the correlations between their local turbulence dynamics and those of the rest of the flow are not significant. In the case of isotropic homogeneous turbulence, this can be done in all three spatial directions. For plane channel flows, this can only be done in the streamwise and spanwise directions. In the normal direction, no-slip conditions are required.

The specification of boundary conditions becomes much more interesting in the case of the flat-plate boundary layer. In this case there is no streamwise periodicity due to the growth of the boundary layer thickness, so something must be assumed for inflow and outflow conditions.

One way to avoid the problem was introduced by Spalart [66], who used a specialised method with additional source terms to simulate the effects of the growth of the boundary layer. This facilitated the use of a streamwise-periodic boundary condition, and the application of spectral discretisations to the streamwise and spanwise directions.

More general approaches range from specifying the turbulent inflow from empirically-calibrated random inputs to the use of full auxiliary channel-flow simulations. The latter technique tends to be more successful than the former, as it minimises the “development” regions in the first portion of the domain associated with the transition from artificially-generated turbulence to that computed by the DNS [41, 38, 30].

Procedures used for dealing with turbulent outflow range from mesh coarsening for the homogenisation of disturbances, to convection-based conditions, to

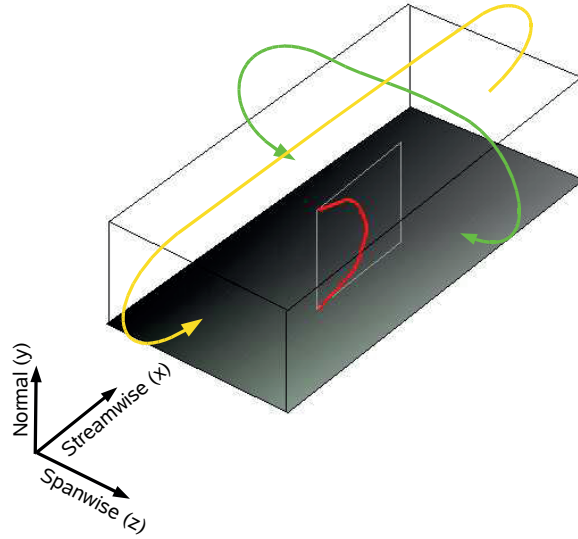


Figure 3.1: The plane channel flow problem (periodic boundary conditions indicated in green and yellow)

sophisticated matched absorption layers. Examples are described in [22, ?, ?].

3.3 DNS Example: Channel flow

Channel flow is the simplest test case for wall-bounded turbulent flows. Since the mean flow is parallel, the turbulence is homogeneous in the stream and spanwise directions. As a result, statistics need only be compared in the wall-normal direction. Channel flow also avoids the problem of having to specify turbulent inflow and outflow conditions, as periodic boundary conditions may be used (figure 3.1). The channel flow contains many of the three-dimensional turbulence dynamics relevant for wall-bounded flows, and recent results show that it still has the capacity to challenge our basic understanding of the physical phenomena.

The first channel DNS was successfully performed by Kim, Moin, and Moser (KMM) in 1987 for $Re_\tau = 180$ (figure 3.2). They used a Fourier spectral method in the stream and spanwise directions, and a Chebyshev polynomial expansion in the normal direction. A semi-implicit scheme was used for time advancement, with Adam-Bashforth for the convective terms and Crank-Nicolson for the viscous terms. The mesh had dimensions of $192 \times 129 \times 160$. In terms of the Kolmogorov scale, this corresponded to a near-wall spacing of $\Delta x = 7.5\eta$, $\Delta y = 0.03\eta$, and $\Delta z = 4.4\eta$. In this case, most of the turbulent energy dissipation occurs at wavelengths above 15η . Relatively large near-wall spacings were chosen as spectral schemes represent waves at the limit of their

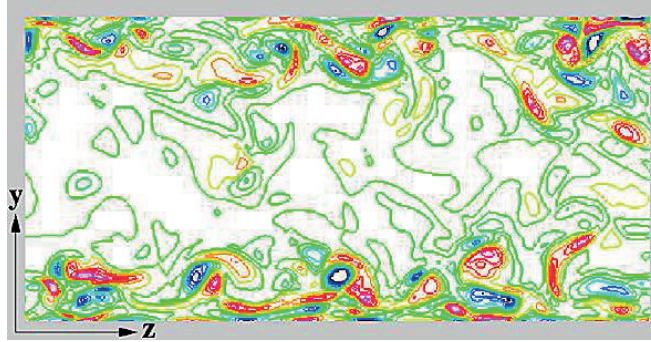


Figure 3.2: Colour contours of the streamwise vorticity, DNS of turbulent channel flow. (J. Kim, P. Moin and R. Moser, J. Fluid Mech. 177, 136-166, 1987, plot: A. Kravchenko)

resolution relatively accurately. If only second-order finite differences are used, similar accuracy would require mesh spacings at least 5 times smaller.

The KMM DNS made a big impact. Firstly, it prompted a critical review of measurements of near-wall turbulence intensity. These were ultimately corrected on the experimental side by the introduction of new measurement techniques. The KMM results also prompted new experiments to search for events which contribute to previously unknown high kurtosis levels (high kurtosis means that the observed variance is due more to infrequent extreme deviations than to frequent moderate deviations). KMM and other channel flow DNS results have also been instrumental in diagnosing deficiencies in Reynolds-averaged turbulence models, which will be discussed in more detail later in these notes.

More recent channel flow computations have taken advantage of both improvements in algorithms and total computational power. Figures 3.3 to 3.5 show results from DNS computations performed over a range of Reynolds numbers by Hoyas and Jiménez on meshes up to $6144 \times 633 \times 4608$. Their scheme used de-aliased Fourier expansions in x and z , and seven-point compact finite differences in y . A third-order Runge-Kutta scheme was used for time advancement.

In wall bounded flows, the near-wall behaviour of streaks and hairpin vortices has been postulated to be universal, implying that the near-wall layer is somewhat insensitive to outer perturbations. This has been implied by mean flow data from experiments, and is superficially supported by inspection of the mean profiles computed for a range of Reynolds numbers by Hoyas and Jiménez. The rms velocity fluctuation profiles (figure 3.5) tell a different story, however. These results, among others, have prompted the recent research on very large coherent structures which modulate the behaviour of the near-wall streaks [42, 62].

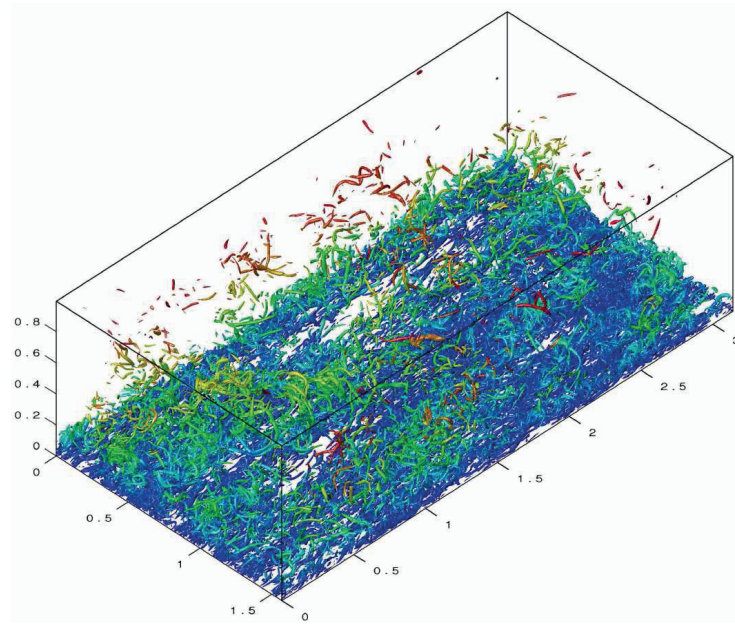


Figure 3.3: Isosurface of the Discriminant of the velocity gradient tensor for an instantaneous realisation of a $Re_{\tau}=1900$ turbulent channel (J.C. del Alamo, J. Jimenez, P. Zandonade and R.D. Moser, J. Fluid Mech. 561, 329-358, 2006.)

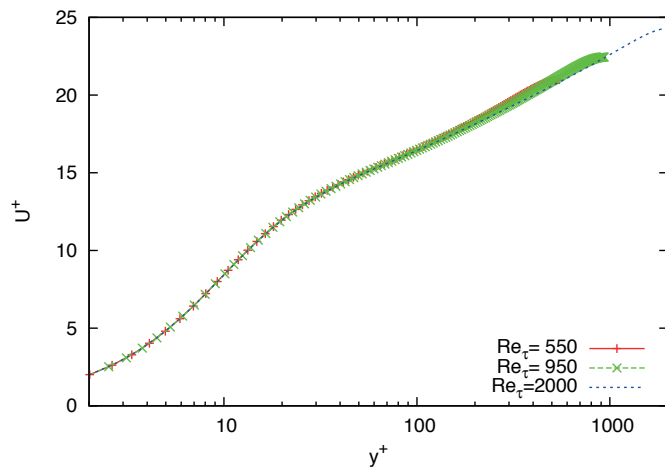


Figure 3.4: Mean profiles in wall units for DNS of turbulent channel flow as a function of Re_{τ} . (S. Hoyas and J. Jiménez. Phys. Fluids 18, 2006)

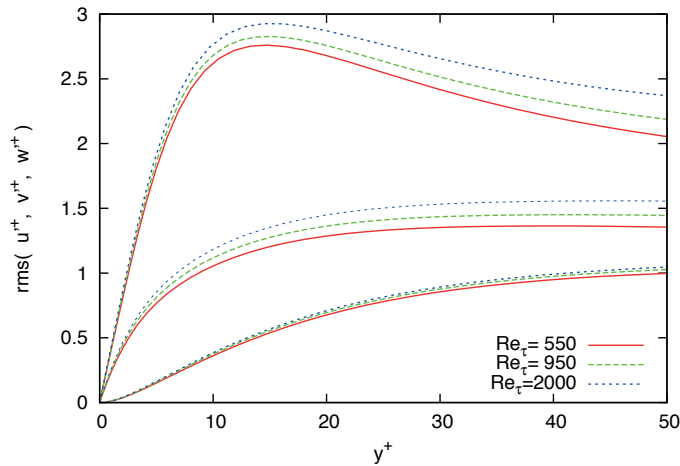


Figure 3.5: rms velocity fluctuations in wall units for DNS of turbulent channel flow as a function of Re_τ . Top group u' , middle group w' , bottom group v' . (S. Hoyas and J. Jiménez. Phys. Fluids 18, 2006)

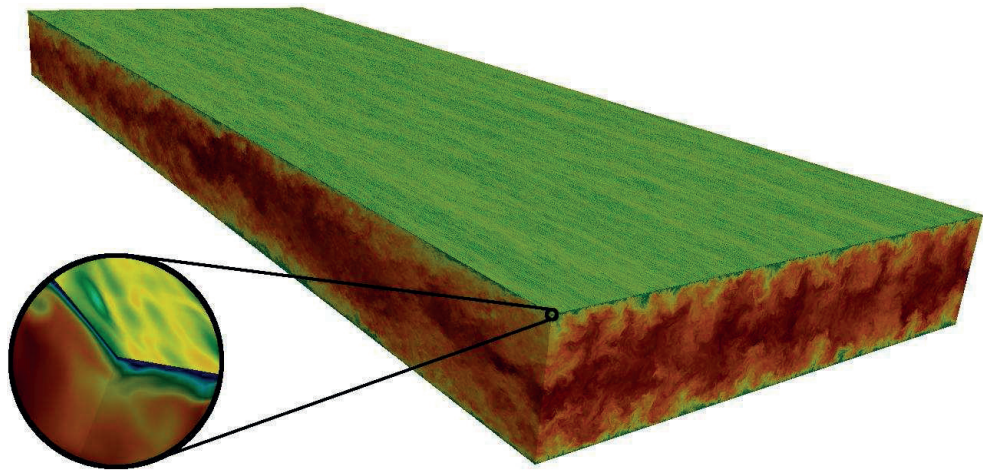


Figure 3.6: DNS of turbulent channel flow at $Re_\tau = 5200$. (Lee and Moser, to appear in J. Fluid Mech. 2015)

Chapter 4

Large-Eddy Simulation

The objective of large-eddy simulation (LES) is to compute the largest scales of turbulent motion, while employing a model for the effects of the smaller scales. The premise behind the method is that it is the largest scales which are affected by the flow conditions and domain boundaries, while smaller scales tend only to be aware of their immediate surroundings and are more likely to behave isotropically, and can thus be easily modelled.

In order to derive governing equations for LES, some method for separating scales is required. In this chapter we will first consider the filtering approach scale separation, which associates a smoothed version of the solution with the larger scales of the flow. Then we will consider variational multiscale methods, where the scales are separated by the choice of solution basis.

4.1 Scale separation using filtering

One way to define a filtered (and therefore large-scale) velocity is to use a convolution over the physical domain, Ω :

$$\bar{u}(x, t) = \int_{\Omega} u(y)G(x - y)dy \quad (4.1)$$

where the convolution kernel should satisfy:

$$\int_{\Omega} G(x - y)dy = 1 \quad (4.2)$$

Examples include the Gaussian filter:

$$G(x) = \sqrt{\frac{6}{\pi\Delta}} \exp\left(-\frac{6x^2}{\Delta^2}\right) \quad (4.3)$$

and the top-hat filter:

$$G(x) = \begin{cases} 1/\Delta & \text{if } |x| \leq \Delta/2 \\ 0 & \text{otherwise} \end{cases} \quad (4.4)$$

where Δ is a parameter which controls the filter width. Another choice is to define filters in spectral space, allowing the use of a sharp cut-off which truncates high-frequency components from the solution:

$$\hat{\bar{u}} = \hat{G}(k)\hat{u} \quad (4.5)$$

here the hat indicates the Fourier transform, k is the wavenumber, and

$$\hat{G}(k) = \begin{cases} 1 & \text{if } k \leq \pi/\Delta \\ 0 & \text{otherwise} \end{cases} \quad (4.6)$$

Note that in general, $\bar{\bar{u}} \neq \bar{u}$.

In many applications LES is actually performed without an explicit filtering operation. In such cases it is the mesh which does the filtering, as it will eliminate all wavelengths shorter than twice the mesh spacing. In this case the filtering effect is more complex, particularly on non-uniform meshes. Therefore the simple filters introduced above are often still employed for the conceptual design of subgrid-scale models.

4.2 The Filtered Navier-Stokes Equations

If we restrict our interest to filtering operations which commute with differentiation, (such as the analytic ones defined in the previous section), we can apply a filter to the incompressible Navier-Stokes equations (A.1) to obtain:

$$\begin{aligned} \frac{\partial \bar{u}_i}{\partial x_i} &= 0 \\ \rho \frac{\partial \bar{u}_i}{\partial t} + \rho \frac{\partial}{\partial x_j} (\bar{u}_i \bar{u}_j) &= -\frac{\partial \bar{p}}{\partial x} + \frac{\partial}{\partial x_j} (\bar{\tau}_{ij} - \rho(\bar{u}_i \bar{u}_j - \bar{u}_i \bar{u}_j)) \end{aligned} \quad (4.7)$$

When the filtering operation is applied, we retain equations of motion for the scales which remain after filtering, \bar{u} . These are the scales which are resolved by a large-eddy simulation. They represent the lowest range of wave numbers, from zero up to some cutoff wavenumber k_c (Figure 4.1).

Due to the non-linear convection term of the Navier-Stokes equations, the dynamics of the resolved scales are not independent of those of the unresolved (sub-filter) scales. The effects of the unresolved scales on \bar{u} are encapsulated in the additional stress-tensor-like term which appears in (4.7), $(\bar{u}_i \bar{u}_j - \bar{u}_i \bar{u}_j) \equiv T_{ij}$. This term is often referred to as the subgrid-stress tensor, due to the prevalence of applications where the filter width is set by the minimum grid size.

Equation (4.7) can not be solved directly, since we lack an expression for T_{ij} . This is known as the closure problem. A model, known as a subgrid-scale (SGS) model, must thus be provided for T_{ij} . Consider a large-eddy simulation carried out for all the scales in a flow up to a cutoff wavenumber, k_c (figure 4.1). Recalling our previous discussion of the kinetic energy cascade, if k_c is sufficiently far from the largest scales of motion we are interested in, then the details of the dynamics of the scales near k_c might not be important. It is important,

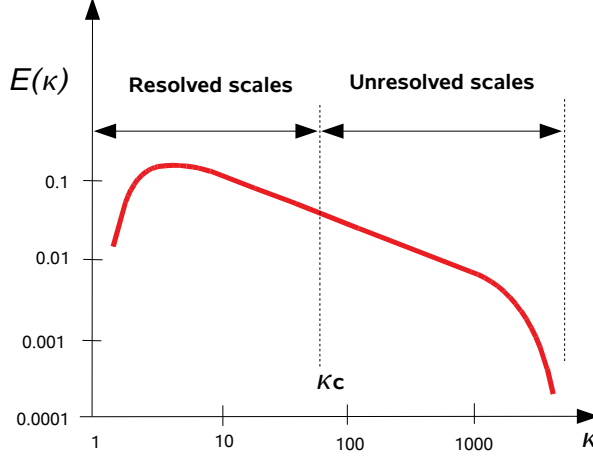


Figure 4.1: Resolved and unresolved scales in LES

however, that the correct amount of turbulent kinetic energy is extracted from the simulation. A common approach is therefore to model the effect of all of the unresolved scales using a dissipative term (although it is in fact only the unresolved scale closest to the Kolmogorov range which actually dissipate the energy). Before pursuing this concept further, however, it is worthwhile first examining the equation for the resolved portion of the kinetic energy.

4.3 The Resolved kinetic energy equation

An equation describing the evolution of the kinetic energy of the resolved scales can be derived by multiplying the filtered momentum equation (4.7) by \bar{u}_i . This results in:

$$\begin{aligned}
 \frac{\partial q}{\partial t} + \underbrace{\frac{\partial}{\partial x_j} (q \bar{u}_j)}_{\text{Advection}} &= - \underbrace{\frac{\partial}{\partial x_i} \left(\frac{\bar{u}_i \bar{p}}{\rho} \right)}_{\text{Pressure diffusion}} \\
 &\quad + \underbrace{\frac{\partial}{\partial x_j} \left(\nu \frac{\partial q}{\partial x_j} \right)}_{\text{Viscous diffusion}} - \underbrace{\nu \frac{\partial \bar{u}_i}{\partial x_j} \frac{\partial \bar{u}_i}{\partial x_j}}_{\text{Viscous dissipation}} \\
 &\quad - \underbrace{\frac{\partial}{\partial x_j} (T_{ij} \bar{u}_i)}_{\text{Diffusion via SGS}} + \underbrace{T_{ij} \bar{S}_{ij}}_{\text{SGS Transfer}} \quad (4.8)
 \end{aligned}$$

where $q = \bar{u}_i \bar{u}_i / 2$, $\nu = \mu / \rho$, and we have exploited the fact that $\frac{\partial \bar{u}_i}{\partial x_i} = 0$ in the re-expression of the terms. The terms on the left hand side are simply

the material derivative of the resolved kinetic energy. The first two terms on the right-hand side represent the redistribution of the resolved kinetic energy due to gradients in pressure and viscous quantities. The third is a pure energy sink corresponding to the resolved viscous stresses. The second-to-last term represents diffusion due to gradients in the unresolved scales. The last term is an energy transfer term which can be instantaneously negative (transfer of energy from resolved to unresolved scales) or positive (backscatter - transfer of energy from unresolved to resolved scales).

4.4 The Smagorinsky model

Boussinesq (1877) postulated that the changes in momentum of the mean flow due to turbulence could be modelled as an additional viscosity, the so-called eddy viscosity, ν_T . Smagorinsky [60] exploited this idea in his 1963 simulations of global weather using large-eddy simulation. In incompressible flow, this amounts to an additional dissipative stress tensor $2\nu_T \bar{S}_{ij}$ which is used to model T_{ij} .

Since $S_{kk} = 0$ in incompressible flow, the Boussinesq assumption restricts us to modelling the deviatoric part¹ of T_{ij} :

$$T_{ij}^D = T_{ij} - \frac{1}{3}\delta_{ij}T_{kk} = -2\nu_T \bar{S}_{ij} \quad (4.9)$$

Since ν_T has the dimensions of velocity multiplied by a length scale, it is modelled as being proportional to the velocity and lengths of the unresolved scales. The largest length of the unresolved scales is given by the filter width, Δ , whereas an estimate for their velocity can be obtained from velocities of the smallest of the resolved scales, which are assumed to be proportional to $\Delta|\bar{S}_{ij}|$. This results in:

$$\nu_T \sim \Delta^2 |\bar{S}_{ij}| \quad (4.10)$$

or

$$\nu_T = (C_s \Delta)^2 |\bar{S}_{ij}| \quad (4.11)$$

where C_s is known as the Smagorinsky constant, and the norm of the strain-rate tensor is normally taken to be $|\bar{S}_{ij}| = (2\bar{S}_{ij}\bar{S}_{ij})^{1/2}$.

It is worth noting that since the ν_T defined by (4.11) is always positive, the Smagorinsky model can only dissipate energy. This is somewhat at odds with the physics, where local energy transfers from smaller to larger scales, known as backscatter, can occur (the energy cascade concept only requires an average energy transfer from large to small scales). The model can still be successful however, if the errors caused by ignoring backscatter are confined to the smallest resolved scales of the computation. The dissipative properties of the Smagorinsky model are also often cited as being helpful for maintaining the stability of numerical solution algorithms.

¹Any stress tensor X_{ij} can be written as a combination of a mean volumetric stress $X_{kk}/3$ and a deviatoric stress tensor, $X_{ij} - \delta_{ij}X_{kk}/3$.

4.4.1 Calibration of the Smagorinsky model

A value for C_s can be derived using the procedure of Lilly [37]. This assumes that the cutoff wavenumber of the computation is in the inertial subrange, and that the cascade process is in equilibrium, that is, the rate of energy transfer from the large scales is instantaneously equal to the rate of energy dissipation of the small scales. The latter can be justified by noting that the reaction time of the small scales is relatively short, and thus they can quickly adjust to any changes in the large scales, which have relatively long characteristic times.

The rate of kinetic energy transfer from the resolved scales to the unresolved scales, ε is given by the last term of (4.8). This is approximated in terms of resolved quantities using the model defined by (4.9):

$$\varepsilon = T_{ij} \bar{S}_{ij} \approx -\nu_T |\bar{S}|^2 \quad (4.12)$$

which is assumed to be equal and opposite to the dissipation of the unresolved scales.

The square of the resolved strain rate can be estimated by:

$$|\bar{S}|^2 = 2 \int_0^{\kappa_c} \kappa^2 E(\kappa) d\kappa \quad (4.13)$$

As this term receives its greatest contributions from higher wave numbers, we can replace $E(\kappa)$ with its desired variation in the inertial subrange, $E(\kappa) = C_K \varepsilon^{\frac{2}{3}} \kappa^{-\frac{5}{3}}$ (equation (2.8)). This leads to

$$|\bar{S}|^2 = \frac{3}{2} C_K \varepsilon^{\frac{2}{3}} \kappa_c^{\frac{4}{3}} \quad (4.14)$$

Substituting (4.12) and (4.11) then re-arranging leads to:

$$C_s = \left(\frac{2}{3C_K} \right)^{\frac{3}{4}} (\kappa_c \Delta)^{-1} \quad (4.15)$$

Usually the filter width, Δ , is chosen to be as small as possible, in order to maximise the resolved-scale range. The highest wave number κ_c which can be resolved on a mesh with spacing h is π/h . Choosing $\Delta = h$ and assuming $C_K = 1.4$ (see chapter 2) gives a value for C_s of 0.18. This value is appropriate for computations of isotropic turbulence, but is often modified to improve the performance of the method for other conditions. For wall-bounded flows, for example, values of $C_s = 0.1$ have been found to be more appropriate.

4.5 Dynamic Modelling

Many turbulent flows of interest are highly inhomogeneous. For such cases employing a constant Smagorinsky coefficient for the entire flow field can be restrictive. Correspondingly, methods have been sought which allow the sub-grid scale model coefficients to vary locally in space and time. Computing these

coefficients as a function of the evolving solution is referred to as dynamic modelling.

A common approach to dynamic modelling is to assume that the basic form of a subgrid-scale model is valid for different cutoff wavenumbers. Consequently, one can derive additional equations by applying the model to multiple grids (or filter widths) which allow consistent model coefficients to be determined. This concept was first introduced by Germano [18] in the context of LES, but it in fact can be applied to any numerical solution procedure where models are used to represent the effects of unresolved scales [4].

To derive a dynamic Smagorinsky model, a second filtering operation is introduced, denoted here by $\tilde{\cdot}$. This “test” filter has a width Δ_t which is wider than that of the primary filter Δ (normally $\Delta_t = 2\Delta$). The objective is to compute a Smagorinsky coefficient assuming that it must have the same local value for both filter widths. Applying a second filter to the filtered Navier-Stokes equations (4.7) results in:

$$\begin{aligned} \frac{\partial \tilde{\tilde{u}}_i}{\partial x_i} &= 0 \\ \rho \frac{\partial \tilde{\tilde{u}}_i}{\partial t} + \rho \frac{\partial}{\partial x_j} (\tilde{\tilde{u}}_i \tilde{\tilde{u}}_j) &= -\frac{\partial \tilde{\tilde{p}}}{\partial x} + \frac{\partial}{\partial x_j} (\tilde{\tilde{\tau}}_{ij} - \rho Q_{ij}) \end{aligned} \quad (4.16)$$

where in this case $Q_{ij} \equiv \widetilde{\tilde{u}_i \tilde{u}_j} - \tilde{\tilde{u}}_i \tilde{\tilde{u}}_j$. If we assume the form of the subgrid-scale model defined by (4.9) and (4.11) is valid over the range considered, we may write:

$$T_{ij} - \frac{1}{3} \delta_{ij} T_{kk} = -2C_d \Delta^2 |\bar{S}_{ij}| \bar{S}_{ij} \quad (4.17)$$

$$Q_{ij} - \frac{1}{3} \delta_{ij} Q_{kk} = -2C_d \Delta_t^2 |\tilde{\bar{S}}_{ij}| \tilde{\bar{S}}_{ij} \quad (4.18)$$

where we have replaced C_s^2 by a dynamic Smagorinsky coefficient C_d , which can become negative, and thus deliver backscatter. We now note that Q_{ij} can also be written:

$$Q_{ij} = \tilde{T}_{ij} + L_{ij} \quad (4.19)$$

where

$$L_{ij} = \widetilde{\tilde{u}_i \tilde{u}_j} - \tilde{\tilde{u}}_i \tilde{\tilde{u}}_j \quad (4.20)$$

(4.17) and (4.18) can then be combined into an explicit relation for C_d :

$$L_{ij} - \frac{1}{3} \delta_{ij} L_{kk} = 2C_d M_{ij} \quad (4.21)$$

where

$$M_{ij} = \Delta^2 |\bar{S}_{ij}| \bar{S}_{ij} - \Delta_t^2 |\tilde{\bar{S}}_{ij}| \tilde{\bar{S}}_{ij} \quad (4.22)$$

The fact that C_d appears ahead of M_{ij} in (4.21) is due to an inconsistent assumption that C_d is “locally constant” for the test filtering operation in (4.20). If this assumption is not used, an alternate method, called dynamic localisation [19], is obtained. Dynamic localisation less frequently employed than the approximate procedure due to the greater computational effort it requires for the determination of C_d .

Equation (4.21) forms an overdetermined system for C_d . It is therefore normal to solve it in the least-squares sense, that is by defining a functional E as:

$$E \equiv \left(L_{ij} - \frac{1}{3} \delta_{ij} L_{kk} - 2C_d M_{ij} \right)^2 \quad (4.23)$$

and requiring $\partial E / \partial C_d = 0$, leading to:

$$C_d = \frac{1}{2} \frac{L_{ij} M_{ij}}{M_{ij}^2} \quad (4.24)$$

which is a minimum since $\partial^2 E / \partial C_d^2 > 0$. Note that this expression illustrates a very desirable property of the dynamic modelling procedure, that C_d will be zero in laminar flow.

When expression (4.24) is used to define C_d , however, the resulting values tend to have both rapid and negative variations in space, which tends to promote numerical instability. In practice it is common to limit C_d to positive values, and smooth its fluctuations. One way of smoothing C_d is to consider instead a functional E_V defined in terms of an integral over a test volume V :

$$E_V \equiv \int_V \left(L_{ij} - \frac{1}{3} \delta_{ij} L_{kk} - 2C_d M_{ij} \right)^2 dV \quad (4.25)$$

leading to:

$$C_d = \frac{1}{2} \frac{\int_V L_{ij} M_{ij} dV}{\int_V M_{ij}^2 dV} \quad (4.26)$$

This approach is particularly effective if the volume can be defined in homogeneous turbulent flow directions, such as in the horizontal planes of a channel flow. A number of more complex smoothing techniques exist for other applications.

4.6 Modern SGS models

The development of SGS models remains an active area of research, and many modern alternatives to the basic static and dynamic models have been developed over the past two decades. The more prominent of these include scale-similarity models which attempt to model components of T_{ij} , one-equation models which employ an additional transport equation for the turbulent kinetic energy, hyper-

and spectral eddy-viscosity models which use alternate formulations for computing and applying the eddy viscosity, and approximate-deconvolution models, which attempt to model the sub-filter scales using a truncated expansion of the inverse filter operator. Model-free LES is also performed, where typically a near-monotone discretisation is used to ensure that high-frequency components of the solution are appropriately damped by the numerical error (this raises the critical issue of how numerical truncation error and subgrid scale models compete with each other to represent the unresolved scales when SGS models are present). See reference [58] for a description of these and other SGS modelling techniques.

4.7 Some example results

It is worthwhile pausing at this point to compare some LES results computed on very coarse meshes to the previous DNS results. Figures 4.2 and 4.3 compare results for incompressible turbulent channel flow at a $Re_\tau = 180$ computed using OpenFOAM.

A range of DNS studies have led to the definition of a minimal flow unit for the channel case [28], with a spanwise extent of 100 wall units and a streamwise extent of approximately 350 units. Experience has shown that in order to capture uncorrelated turbulent flow behaviour, however, several of these units should be included in the simulation. For $Re_\tau = 180$, a channel with a span of two times its height, and a length of three times its height is used, which corresponds to dimensions of 720 and 1080 in wall units, respectively. No-slip boundary conditions are applied on the top and bottom walls, and periodic boundary conditions are used in the streamwise and spanwise directions. The flow is driven by a constant source term. Using periodic boundary conditions avoids the problem of providing models for the inflow and outflow regions, but can also lead to correlations which affect turbulence dynamics

The calculations were performed on a sequence of meshes, ranging in x, y, z dimension from $32 \times 32 \times 32$ to $64 \times 64 \times 64$. The basic method is a second-order accurate central finite-volume scheme, with second-order accurate implicit time integration. As this flow is far from isotropic, the constant-coefficient Smagorinsky model (“Smag”) still requires more resolution, although there is a considerable improvement from 32^3 to 64^3 . Also shown are results from a static one-equation model, although these are not significantly better at coarse levels of resolution. The dynamic Smagorinsky model (“dynSmag”), on the other hand, matches the mean profile well at 32^3 , and converges to the rms fluctuations at slightly higher levels of resolution. This improvement in performance comes at a cost increase of around 15%, so it is definitely effective in this case.

4.8 LES of wall-bounded flows

“In the viscous near-wall region, there are no large eddies”

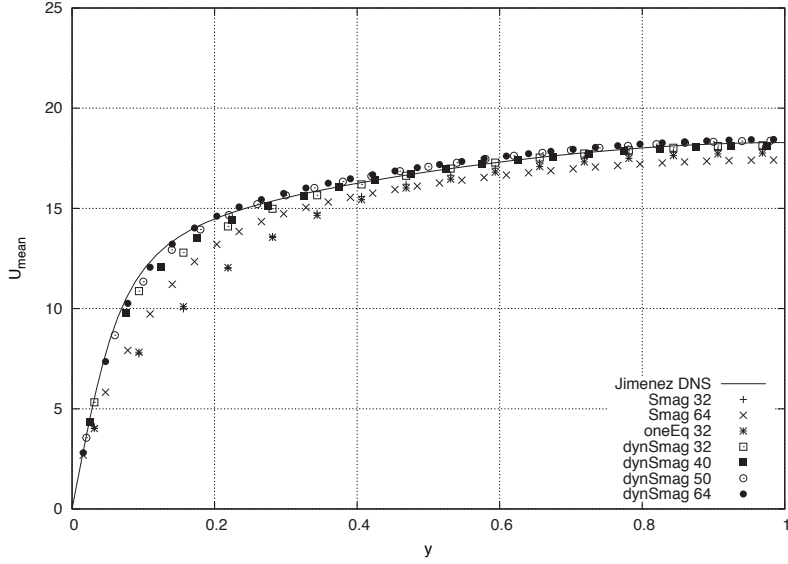


Figure 4.2: Mean velocity profile obtained using static and dynamic subgrid scale models at different mesh resolutions (Computed by I. Popov NEQLab/TU Delft)

(attributed to Bradshaw in [54]).

The cost of LES is independent of Reynolds number for homogenous isotropic turbulence, since all that is necessary to correctly predict the large energy-containing scales is to resolve the first part of the inertial range. Homogenous isotropic turbulence is very relevant to the development of turbulence theory, but it is rarely encountered in applications. Turbulent wall-bounded flows are of far greater practical interest, particularly since the energy lost due to their associated dissipation has significant economic impact.

As mentioned in chapter 2, the maximum of turbulent energy production occurs in wall bounded flows occurs in the buffer layer. The main contributing dynamics are those of the low and high-speed streaks, which dimensions on the order of $x^+ = 1000$, $y^+ = 30$, $z^+ = 100$. These units scale inversely with Reynolds number, so maintaining sufficient resolution in space and time becomes increasingly difficult as higher Reynolds numbers are considered. In fact Pope [54] estimated that the number of streaks on a modern airliner is approximately 10^8 , which results in memory and computing requirements well above current computing capacities.

Piomelli [51] performed a detailed analysis of the scaling of the resolution requirements for LES of turbulent boundary layers. He found that if the inner layer is to be resolved, then the number of grid points requires scales with

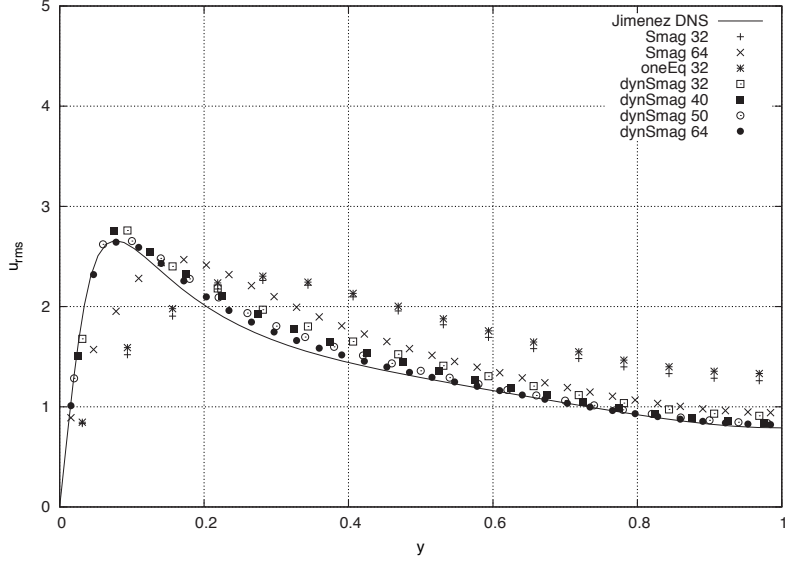


Figure 4.3: rms streamwise fluctuation profile obtained using static and dynamic subgrid scale models at different mesh resolutions (Computed by I. Popov NEQLab/TU Delft)

$Re^{2.4}$. If only the outer layer is to be resolved, however, the scaling is $Re^{0.6}$. This provides significant motivation for Pope's question "Do we really need to compute all those steaks?".

The result has been the development of several approaches to near-wall modelling, which may be broadly divided into wall-stress and hybrid methods. One of the first successful wall-stress methods was the wall-stress equilibrium model of Schumann [59], who placed his first off-wall points in the logarithmic layer, and used the velocity at these points combined with empirical law-of-the-wall profiles to provide an estimate for the instantaneous wall stress at the boundary. A more recent version of this approach was developed by Nicoud [48], in which sub-optimal control is employed to determine wall conditions which minimise deviations from a cost function incorporating the desired mean and rms fluctuation profiles.

Hybrid techniques, on the other hand, typically make use of the solution of another set of model equations in a region near the wall. In zonal hybrid methods, a distinct near-wall region is defined in which the turbulent boundary layer or Reynolds-averaged equations are solved. This is connected to the outer LES region through explicit boundary conditions. In blended hybrid methods, a smooth transition is made from regions where the unsteady Reynolds-averaged equations are solved to those where a standard LES is performed (an example is the DES method of Spalart [68, 64]). Both zonal and blended approaches

suffer from transition layers resulting from their interface treatment [52], yet have produced useful results.

In summary, wall-modelling techniques have made a substantial impact on the practicality of using LES for realistic applications, and remain a relevant and active area of research.

4.9 Subtle Issues with Filter-Based Techniques

The filter-based view of LES raises some subtle but important issues. The first of these stems from the assumption that filtering and differentiation commute. For the standard filters considered in LES, this is only true on uniform meshes. In practical applications, however, stretched meshes are frequently required. Near the boundaries of a flow domain, filtering operations must also be non-uniform, as the local stencil is necessarily one-sided. If a standard LES filter is used under these conditions, the derivation of the original filtered Navier-Stokes equations is invalid due to “commutation errors”. Although sometimes ignored, commutation errors present significant conceptual problems for methods which require the explicit definition of a filter (such as approximate-deconvolution models). Correspondingly, the design of filters for non-uniform filter widths has received significant attention.

As previously pointed out, however, most calculations use the mesh as a filter rather than performing explicit filtering. This is done in order to maximise the resolution available for the physical process. Doing so, however, raises another issue. When explicit filtering is used, it is possible to keep the filter width constant and vary the mesh size in order to quantify the effects of numerical discretisation errors. If instead the mesh is used as a filter, the numerical discretisation errors will have the same length scales as the SGS model, making their influence difficult to separate from that of the model.

There have been a number of approaches to dealing with this issue. Firstly, if the SGS model is designed to be purely dissipative, then the basic numerical scheme can be chosen to be as non-dissipative as possible, normally by using central discretisations, or more formally by deriving kinetic-energy conserving schemes. Another approach is to use a higher-order accurate numerical method, although this is no panacea, as the truncation error of higher-order methods is not necessarily small if the mesh is coarse relative to the gradients being resolved. Since in LES there is often significant energy near k_c , higher-order scheme must be designed to have low absolute error as well.

A more integrated approach is to explicitly combine the design of the SGS model with that of the numerical scheme. An example is the MILES scheme, where the dissipative components of the flux definition for a (near-) monotone conservative finite-volume scheme are scaled to account for turbulent subgrid dissipation [21]. An alternative is to consider the design of SGS models in a variational multiscale framework, which naturally unites the concepts of truncation errors and subgrid-scale modelling. This approach is considered in the following sections.

4.10 The Multiscale Approach to LES

The crucial factor for determining the success of LES methods is the representation of what is not computed, i.e. the unresolved scales. From the multiscale viewpoint, the unresolved scales are directly defined by the choice of basis used to represent the resolved scales. This relationship illustrated in figure 4.4 (a) for a spectral method representing the resolved solution, \bar{u} , with a single wave number , and in figure 4.4 (b) for a finite-element solution representing \bar{u} with piecewise-linear functions. Here u is the complete solution, \bar{u} is the resolved solution and u' is the unresolved solution, such that $u = \bar{u} + u'$.

In general u is defined by an infinite set of functions, \mathcal{V} . For example, in a Fourier decomposition of u , \mathcal{V} would contain sines and cosines from wavenumbers $k = 0$ to ∞ . For multiscale LES we wish to compute \bar{u} , the part of the solution that lives in a truncated version of \mathcal{V} , which we denote as $\bar{\mathcal{V}}$. Thus, u' is the part of u that lives in the set of remaining functions $\mathcal{V}' = \mathcal{V} - \bar{\mathcal{V}}$. For example, if we choose $\bar{\mathcal{V}}$ to be a set of low- k sinusoids (a spectral method) u' will live in a \mathcal{V}' defined in terms the remaining high- k sinusoids. If we choose $\bar{\mathcal{V}}$ to be piecewise linear functions (as in a finite-element method) u' will live in a \mathcal{V}' which contains functions which have discontinuous derivatives at element interfaces (C^0 functions). In both cases \mathcal{V}' , is infinite-dimensional.

Solving for u' would require infinite computing resources, so clearly it must be approximated. The goal of multiscale LES is to approximate u' such that the the resolved scales represent \bar{u} (not u) as accurately as possible.

4.10.1 Analysis of a general problem

The basic approach of the variational multiscale method can be illustrated with the following general problem:

$$\mathcal{L}u = f \quad \text{in } \Omega, \tag{4.27}$$

$$u = g \quad \text{on } \Gamma \tag{4.28}$$

where \mathcal{L} is an arbitrary differential operator (which could be the Navier-Stokes operator, for example), and Γ denotes the boundary of the domain Ω . To solve this problem via the method of weighted residuals, we introduce a weighting function w , also chosen from an infinite set, \mathcal{W} , and define the variational form of the problem as:

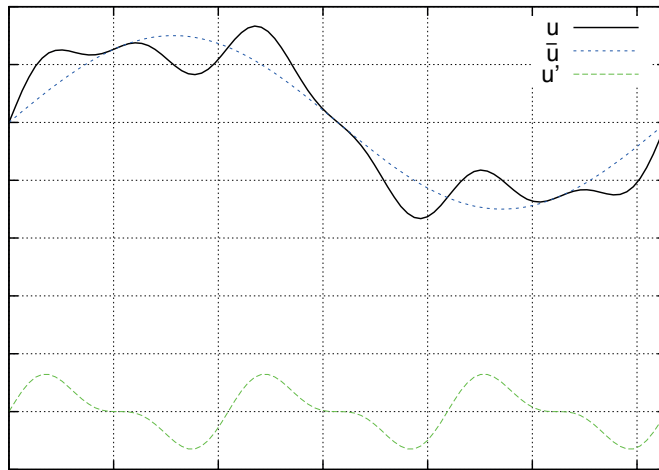
$$\int_{\Omega} w \mathcal{L}u \, d\Omega = \int_{\Omega} w f \, d\Omega \tag{4.29}$$

or in compact notation (see the appendix of part 1):

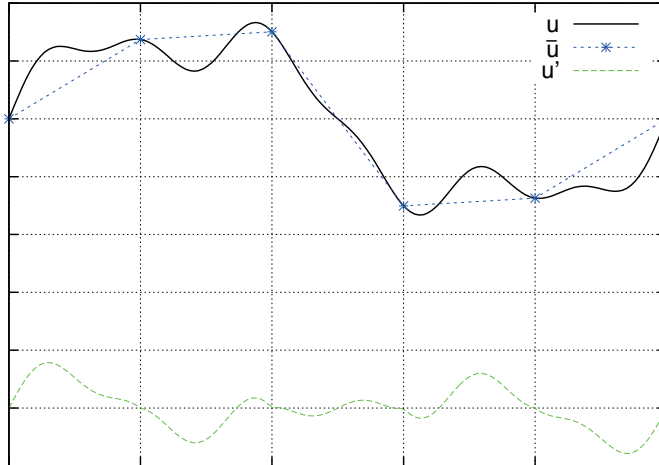
$$(w, \mathcal{L}u)_{\Omega} = (w, f)_{\Omega} \tag{4.30}$$

$$u = g \quad \text{on } \Gamma \quad \forall u \in \mathcal{V} \tag{4.31}$$

$$w = 0 \quad \text{on } \Gamma \quad \forall w \in \mathcal{W} \tag{4.32}$$



(a) Spectral method



(b) Finite-element method

Figure 4.4: Resolved and unresolved scales from the multiscale viewpoint

Now we consider the partitioned solution $u = \bar{u} + u'$. In a Galerkin solution procedure, we express the approximation for the resolved scales as $\bar{u} = \sum_i^N a_i \bar{\phi}_i$ where $\bar{\phi}_i$ spans $\bar{\mathcal{V}}$. In order to solve for the unknown amplitudes a_i , we write (4.29) for N test functions. We thus partition the weighting space as $w = \bar{w} + w'$ where \bar{w} is finite-dimensional, and contains the N functions necessary to solve for the $N a_i$. We can then write the weak form for the resolved scales as:

$$(\bar{w}, \mathcal{L}(\bar{u} + u'))_\Omega = (\bar{w}, f)_\Omega \quad [\text{resolved-scale equations}] \quad (4.33)$$

which results in a system of N equations. Unfortunately this system is incomplete, as u' is unknown. With infinite computing resources, we could solve u' by writing

$$(w', \mathcal{L}(\bar{u} + u'))_\Omega = (w', f)_\Omega \quad [\text{unresolved-scale equations}] \quad (4.34)$$

for all functions in the infinite-dimensional set w' . Instead, we use approximations of u' inspired by the unresolved-scale equations (4.34). Note that the unresolved-scale equations can also be written

$$(w', \mathcal{L}u' + \mathcal{N}(\bar{u}, u'))_\Omega = -(w', \mathcal{L}u - f)_\Omega \quad (4.35)$$

$$= (w', -\mathcal{R}) \quad (4.36)$$

where \mathcal{N} contains terms with both \bar{u} and u' arising from the nonlinear part of \mathcal{L} , and $\mathcal{R} = \mathcal{L}u - f$ is the residual of the resolved scales. This equation implies that the unresolved solution is driven by the residual of the resolved solution. In fact we will seek approximations for u' which are zero when $\mathcal{R} = 0$. This will ensure that when the complete solution u , can be captured by \bar{u} (which implies f is also in $\bar{\mathcal{V}}$), then u' is zero and (4.33) is exact.

It is worth pausing to reflect on how discretisation and unresolved-scale modelling errors appear in this framework. For LES, that our goal is to compute only the part of u which lives in $\bar{\mathcal{V}}$. Since we have made no approximation in the derivation of (4.33), all of the error in \bar{u} is due to the approximation of u' . Thus in multiscale LES, there is no distinction between discretisation and unresolved-scale model errors. Setting $u' = 0$ will produce the classical errors associated with using a Galerkin solution procedure, but will see that better approximations for u' can attenuate or even eliminate errors in \bar{u} .

4.10.2 Approximation of u' for linear advection

To demonstrate the philosophy behind deriving approximations for u' , we consider the steady linear advection-diffusion equation in 1D.

$$\mathcal{L}u = f \quad \text{in } \Omega, \quad (4.37)$$

$$u = g \quad \text{on } \Gamma \quad (4.38)$$

$$\mathcal{L} = c \frac{\partial}{\partial x} - \nu \frac{\partial^2}{\partial x^2} \quad (4.39)$$

As the equation is linear, $\mathcal{N} = 0$ and the resolved and unresolved scale equations are just:

$$(\bar{w}, \mathcal{L}\bar{u})_\Omega + (\bar{w}, \mathcal{L}u')_\Omega = (\bar{w}, f)_\Omega \quad [\text{resolved}] \quad (4.40)$$

$$(w', \mathcal{L}u')_\Omega = (w', -\mathcal{R})_\Omega \quad [\text{unresolved}] \quad (4.41)$$

We assume that g is in $\bar{\mathcal{V}}$ so that $\bar{u} = g$ and $u' = 0$ on the boundary Γ . Since these are both Dirichlet conditions, $\bar{w} = w' = 0$ on Γ . We can then use integration by parts to re-express the unresolved advection and diffusion terms as:

$$(w, cu'_x)_\Omega = wcu' |_\Gamma - (w_x, cu')_\Omega = -(w_x, cu')_\Omega \quad (4.42)$$

and

$$(w, -\nu u'_{xx})_\Omega = -w\nu u'_x |_\Gamma + (w_x, \nu u'_x)_\Omega = (w_x, \nu u'_x)_\Omega \quad (4.43)$$

$$= w_x \nu u' |_\Gamma - (w_{xx}, \nu u')_\Omega = -(w_{xx}, \nu u')_\Omega \quad (4.44)$$

Noting that the adjoint operator, T^* , of an operator T is defined such that $(a, Tb) = (T^*a, b)$, the resolved- and unresolved-scale equations are then:

$$(\bar{w}, \mathcal{L}\bar{u})_\Omega + (\mathcal{L}^*\bar{w}, u')_\Omega = (\bar{w}, f)_\Omega \quad [\text{resolved}] \quad (4.45)$$

$$(\mathcal{L}^*w', u')_\Omega = (w', -\mathcal{R})_\Omega \quad [\text{unresolved}] \quad (4.46)$$

where \mathcal{L}^* is the advection-diffusion adjoint operator

$$\mathcal{L}^* = -c \frac{\partial}{\partial x} - \nu \frac{\partial^2}{\partial x^2} \quad (4.47)$$

Now we consider the 1D finite-element case shown in 4.5, where \bar{u} is expressed as a piecewise linear solution that matches u at the nodes. The unresolved-scale equation is to be applied to the entire domain Ω , and therefore must deal with the fact that at the element edges, there are jumps in the derivatives of u' . This ‘‘rough’’ case can be dealt with by performing integration by parts element-wise, and retaining the Γ_e terms to account for the jumps in u'_x at the element boundaries [25]. Alternatively, we can avoid this issue by choosing only to solve approximate problems for the unresolved scales localised within each element, e . This is far more practical, as then we can treat one element as a time (as is traditional in finite-element methods), and a sparse system of equations produced, which can be solved much more efficiently than a full system. Furthermore, this approximation does not necessarily prevent us from achieving a nodally exact \bar{u} .

We thus consider the solution for u' on Ω_e with zero Dirichlet boundary conditions on Γ_e . This can be expressed in terms of an *element Green’s function*, g'_e , defined by the problem:

$$\mathcal{L}^*g'_e(x, y) = \delta(x - y) \quad \text{in } \Omega_e \quad (4.48)$$

$$g'_e(x, y) = 0 \quad \text{on } \Gamma_e \quad (4.49)$$

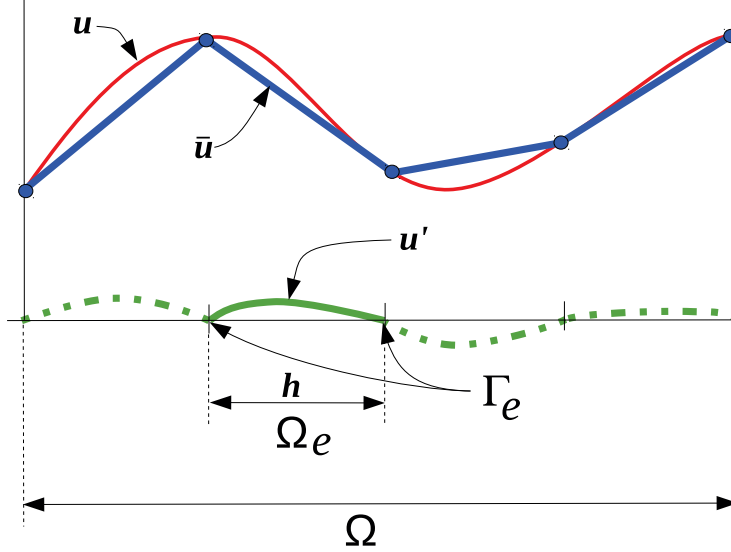


Figure 4.5: Nomenclature for 1D Multiscale analysis

This allows u' to be expressed as:

$$u'(y) = - \int_{\Omega} g'_e(x, y) \mathcal{R}(x) d\Omega_x \quad (4.50)$$

For advection-diffusion, an exact element Green's function can be found:

$$g'_e(x, y) = \begin{cases} C_1(y)(1 - e^{-2\alpha \frac{x}{h}}), & x \leq y \\ C_2(y)(e^{-2\alpha \frac{x}{h}} - e^{-2\alpha}), & x \geq y \end{cases} \quad (4.51)$$

where h is the length of the element and

$$C_1(y) = \frac{1 - e^{-2\alpha(1 - \frac{y}{h})}}{a(1 - e^{-2\alpha})} \quad (4.52)$$

$$C_2(y) = \frac{e^{2\alpha \frac{y}{h}} - 1}{a(1 - e^{-2\alpha})} \quad (4.53)$$

$$\alpha = \frac{ch}{2\nu} \quad (4.54)$$

Substituting the expression for u' into the resolved-scale equation gives:

$$(\bar{w}, \mathcal{L}\bar{u} - f)_{\Omega} + \sum_e \int_{\Omega_e} \mathcal{L}^* \bar{w}(y) \left(\int_{\Omega_e} g'_e(x, y) \mathcal{R}(x) d\Omega_x \right) d\Omega_y = 0 \quad (4.55)$$

In 1D, this expression produces a nodally-exact \bar{u} , independent of the element size, h .

At this point we note that for a Bubnov-Galerkin method with piecewise linear functions, $w_{xx} = 0$. Therefore $\mathcal{L}^* \bar{w} = -cw_x$. If the sign of this term is changed, and added to the \bar{w} test of the residual in the first term of (4.55), we have the SUPG method. This suggests defining τ as:

$$\tau = \frac{1}{h} \int_{\Omega_e} \int_{\Omega_e} g'_e(x, y) d\Omega_x d\Omega_y \quad (4.56)$$

$$= \frac{h}{2c} \left(\coth \alpha - \frac{1}{\alpha} \right) \quad (4.57)$$

Noting that $\mathcal{L}\bar{u}$ and $\mathcal{L}^*\bar{w}$ are constant over an element with piecewise linear functions, the resolved-scale equation is then:

$$(\bar{w}, \mathcal{L}\bar{u} - f)_\Omega - \sum_e \int_{\Omega_e} \mathcal{L}^*\bar{w} \tau \mathcal{R}(x) d\Omega = 0 \quad (4.58)$$

which in this case is equivalent to SUPG, with a τ which gives the nodally-exact solution, independent of h . This also implies the approximation for the unresolved scales (as far as the resolved-scale equation is concerned) is:

$$u' \approx -\tau \mathcal{R} \quad (4.59)$$

This will approximation will be locally incorrect within the element due to operations such as (4.56), but will still produce the exact \bar{u} when integrated as in (4.58).

4.10.3 An implementation for LES

In this case we consider a problem based on the incompressible Navier-Stokes equations, here written in vector form:

$$\frac{\partial \mathbf{u}}{\partial t} + \nabla \cdot (\mathbf{u} \otimes \mathbf{u}) + \frac{\nabla p}{\rho} - \nabla \cdot 2\nu \nabla^s \mathbf{u} = f \quad \text{in } \Omega \quad (4.60)$$

$$\nabla \cdot \mathbf{u} = 0 \quad \text{in } \Omega \quad (4.61)$$

$$\mathbf{u} = 0 \quad \text{on } \Gamma \quad (4.62)$$

$$\int_\Omega p d\Omega = 0 \quad \forall t \in]0, T[\quad (4.63)$$

where ρ is constant and $\nabla^s \mathbf{u}$ is the symmetric velocity gradient (S_{ij} in appendix A.1). A variational form of the problem can be obtained by testing the momentum equations with the vector of weighting functions \mathbf{w} and continuity with the weighting function q . As before, however, we decompose $\mathbf{u} = \bar{\mathbf{u}} + \mathbf{u}'$ and $p = \bar{p} + p'$, as well as $\mathbf{w} = \bar{\mathbf{w}} + \mathbf{w}'$ and $q = \bar{q} + q'$ such that the resolved-scale problem can be written:

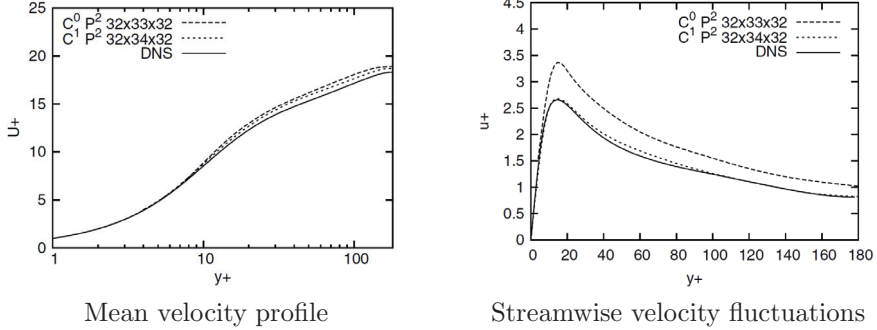


Figure 4.6: Results for multiscale LES of turbulent channel flow

Find $\{\bar{\mathbf{u}}, \bar{p}\} \in \bar{\mathcal{V}}$ such that for all $\{\bar{\mathbf{w}}, \bar{q}\} \in \bar{\mathcal{V}}$

$$\begin{aligned} \left(\bar{\mathbf{w}}, \frac{\partial \bar{\mathbf{u}}}{\partial t} \right)_\Omega &= (\nabla \bar{\mathbf{w}}, \bar{\mathbf{u}} \otimes \bar{\mathbf{u}})_\Omega - (\nabla \cdot \bar{\mathbf{w}}, \frac{\bar{p}}{\rho})_\Omega + (\nabla^s \bar{\mathbf{w}}, 2\nu \nabla^s \bar{\mathbf{u}})_\Omega \\ + \left(\bar{\mathbf{w}}, \frac{\partial \mathbf{u}'}{\partial t} \right)_\Omega &= (\nabla \bar{\mathbf{w}}, \bar{\mathbf{u}} \otimes \mathbf{u}')_\Omega - (\nabla \bar{\mathbf{w}}, \mathbf{u}' \otimes \bar{\mathbf{u}})_\Omega - (\nabla \bar{\mathbf{w}}, \mathbf{u}' \otimes \mathbf{u}')_\Omega \\ &\quad - (\nabla \cdot \bar{\mathbf{w}}, \frac{p'}{\rho})_\Omega + (\nabla^s \bar{\mathbf{w}}, 2\nu \nabla^s \mathbf{u}')_\Omega \\ &= (\bar{\mathbf{w}}, f)_\Omega , \\ (\bar{q}, \nabla \cdot \bar{\mathbf{u}}) &+ (\bar{q}, \nabla \cdot \mathbf{u}') = 0 \end{aligned} \quad (4.64)$$

The $(\nabla^s \bar{\mathbf{w}}, 2\nu \nabla^s \mathbf{u}')$ is usually omitted as argued in [1]. The $(\bar{\mathbf{w}}, \frac{\partial \mathbf{u}'}{\partial t})$ term is often neglected with the assumption that the unresolved scales respond relatively quickly, making a quasi-steady approximation appropriate. There are, however, advantages including this term, as discussed in [10, 55]. Other than these modifications, the interaction terms with the unresolved scales remain exact. Once again the unresolved-scale equations can be used to form approximations for \mathbf{u}' and p' . In principle the coupled unresolved-scale momentum and continuity system should be solved, but even decoupled approximations, such as $u'_i = -\tau_m \mathcal{R}_{m_i}$ and $p' = -\tau_c \mathcal{R}_c$, (where \mathcal{R}_{m_i} are the momentum equation residuals and \mathcal{R}_c is the continuity equation residual) can be quite effective.

Results from [3] using such decoupled expressions for \mathbf{u}' and p' for the case of turbulent channel flow are shown in figure 4.6. Two types of quadratic basis were used. The first of these was a classic C^0 continuous finite-element basis as shown in 4.7 left. The second was a C^1 continuous quadratic NURBS basis as shown in 4.7 right. Both had just over $32 \times 32 \times 32$ degrees of freedom (the differences have to do with the form of the functions near the boundary). The C^1 continuous results are particularly good, being comparable to the $64 \times 64 \times 64$ dynamic Smagorinsky results presented earlier in this chapter. These likely benefit by reducing the magnitude of the ‘‘rough’’ terms neglected in the derivation of u' and p' .

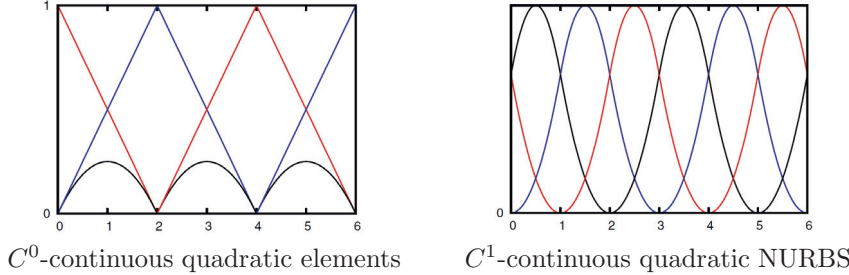


Figure 4.7: Basis functions for multiscale LES of turbulent channel flow

In general, these results illustrate that variable multiscale discretisations are effective for LES, while delivering some theoretical benefits. Notably, they avoid the difficulties associated with the filtering concept on anisotropic meshes and near boundaries. Also, as the equations are exact when $u \in \mathcal{V}$, they do not introduce significant modelling into laminar regions of the flow. Finally, as the unresolved-scale interaction terms remain unaltered, they provide a framework for developing sophisticated models of unresolved scales, including those with local backscatter.

4.10.4 A three-scale VMM

The Smagorinsky LES results presented earlier in the chapter differ from those of the last section in that the unresolved-scale model, being instantaneously proportional to the local strain-rate tensor, does have the same form as the exact unresolved-scale interaction terms. Furthermore, it is not residual-based, so it remains active in the regions of the flow which are dominated by larger scales. Insight into these effects can be gained by separating the latter from the former, which can be done using a three-scale multiscale technique.

The initial LES technique introduced by Hughes [24] can be interpreted as a three-scale VMM [11]. To formulate it, we will divide the complete scale range into large resolved scales, small resolved scales, and unresolved scales (figure 4.8). Having two ranges of resolved scales provides flexibility in the application of unresolved-scale models which can be advantageously exploited when computing turbulent flows.

To demonstrate the approach, we will consider a space-time discretisation for the compressible Navier-Stokes equations. In space-time discretisations, 4D sub-domains are considered, where the 4th dimension (time) has the width of a single time step Δt (an analogous 2D-space (3D space-time) example is shown in figure 4.9). To march in time, we solve the solution on a given sub-domain Q_n (often called a “slab”) and then impose the solution on the upper time boundary of Q_n as a boundary condition for Q_{n+1} . Considering the problem in space-time simplifies the discussion somewhat, as the time march need not be considered separately. Space-time discretisations also provide a lot of flexibility

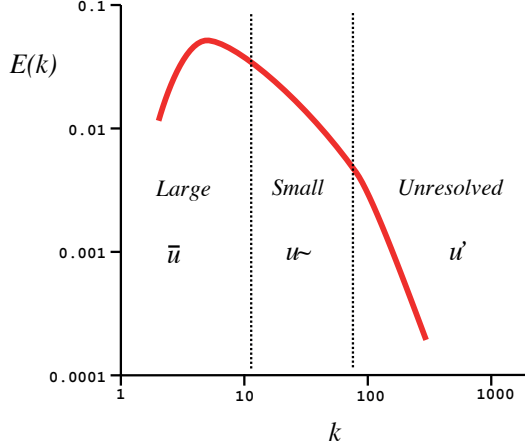


Figure 4.8: Kinetic energy cascade divisions for three-scale VMM

for moving or adapting meshes, although this flexibility normally comes at a higher computational cost. To make our notation as compact as possible, we will use the following short forms:

- $A_{i,j}$: Component i of A differentiated in the j direction
- $A_{,t}$: A differentiated with respect to time
- $(A, B)_C$: Integral of the product $A B$ over the domain C

The compressible Navier-Stokes equations, written in terms of the conservation variables $\mathbf{U} = \{\rho, \rho\mathbf{u}, \rho E\}$ (specific mass, momentum, and energy) are then :

$$\mathbf{U}_{,t} + \mathbf{F}_{i,i} - \mathbf{F}_{i,i}^v = \mathbf{S} \quad (4.65)$$

where $\mathbf{F} = \mathbf{F}(\mathbf{U})$ and $\mathbf{F}^v = \mathbf{F}^v(\mathbf{U})$ are the inviscid and viscous fluxes, and \mathbf{S} is a source term.

In order to construct a variational form of (4.65), we multiply by a weighting function, W , and integrate over the space-time domain Q_n . The problem of finding \mathbf{U} can then be expressed:

Find $\mathbf{U} \in \mathcal{V}_n$ such that $\forall \mathbf{W} \in \mathcal{W}_n$

$$\begin{aligned} & - (\mathbf{W}_{,t}, \mathbf{U})_{Q_n} - (\mathbf{W}_{,i}, \mathbf{F}_i - \mathbf{F}_i^v)_{Q_n} \\ & + (\mathbf{W}, (\mathbf{F}_i - \mathbf{F}_i^v) n_i)_{P_n} + (\mathbf{W}(t_{n+1}), \mathbf{U}(t_{n+1}))_{\Omega_{n+1}} \\ & - (\mathbf{W}(t_n), \mathbf{U}(t_n))_{\Omega_n} = (\mathbf{W}, \mathbf{S})_{Q_n} \end{aligned} \quad (4.66)$$

where \mathcal{V}_n and \mathcal{W}_n are finite-dimensional subspaces (normally local polynomials defined on an element or group of elements). To derive (4.66), we have used integration by parts to avoid taking the gradient of the flux terms, resulting in

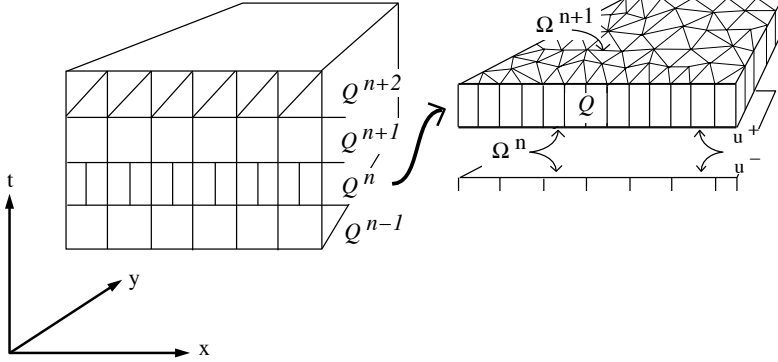


Figure 4.9: Space-time domain

an additional boundary integral along the edges, P_n , of the space-time slab Q_n , with local surface normal n_i . (4.66) can be expressed compactly as:

$$B(\mathbf{W}, \mathbf{U}) = (\mathbf{W}, \mathbf{S}) \quad (4.67)$$

So that we can identify the scales within the discretisation, we divide the interpolation and weighting functions into three levels [24, 11, 46]:

$$\mathbf{U} = \overline{\mathbf{U}} + \widetilde{\mathbf{U}} + \mathbf{U}', \quad \mathbf{W} = \overline{\mathbf{W}} + \widetilde{\mathbf{W}} + \mathbf{W}' \quad (4.68)$$

Here $\overline{\mathbf{U}}$ are the large resolved scales, $\widetilde{\mathbf{U}}$ are the small resolved scales and \mathbf{U}' are the unresolved scales. As we assume that $\overline{\mathbf{W}}$ and $\widetilde{\mathbf{W}}$ are linearly independent, we can write large and small resolved scale equations as:

$$\text{Large: } B(\overline{\mathbf{W}}, \overline{\mathbf{U}} + \widetilde{\mathbf{U}} + \mathbf{U}') = (\overline{\mathbf{W}}, \mathbf{S}) \quad (4.69)$$

$$\text{Small: } B(\widetilde{\mathbf{W}}, \overline{\mathbf{U}} + \widetilde{\mathbf{U}} + \mathbf{U}') = (\widetilde{\mathbf{W}}, \mathbf{S}) \quad (4.70)$$

where for example, the large-scale equation can be expanded as:

$$\begin{aligned} B(\overline{\mathbf{W}}, \overline{\mathbf{U}}) + B'(\overline{\mathbf{W}}, \overline{\mathbf{U}}, \widetilde{\mathbf{U}}) - R(\overline{\mathbf{W}}, \widetilde{\mathbf{U}}) &= (\overline{\mathbf{W}}, \mathbf{S}) \\ - B'(\overline{\mathbf{W}}, \overline{\mathbf{U}}, \mathbf{U}') + R(\overline{\mathbf{W}}, \mathbf{U}') + C(\overline{\mathbf{W}}, \widetilde{\mathbf{U}}, \mathbf{U}') &, \end{aligned} \quad (4.71)$$

Here $B'(\overline{\mathbf{W}}, \overline{\mathbf{U}}, \mathbf{U}')$ is the $B(\overline{\mathbf{W}}, \overline{\mathbf{U}})$ operator linearised about $\overline{\mathbf{U}}$ for a perturbation \mathbf{U}' , $C(\overline{\mathbf{W}}, \widetilde{\mathbf{U}}, \mathbf{U}')$ contains generalised cross stresses, and $R(\overline{\mathbf{W}}, \widetilde{\mathbf{U}})$ contains generalised Reynolds stresses. We could also write equations for the unresolved scales, but in this case we will be replacing \mathbf{U}' terms with a Smagorinsky model, so the additional equations are not required.

In order to link $\overline{\mathbf{W}}$ and $\widetilde{\mathbf{W}}$ to the idea of large and small resolved scales, hierachal bases are used for \mathcal{V}_n and \mathcal{W}_n (figure 4.10). The individual components of these bases are divided in terms of their length scales, with the largest

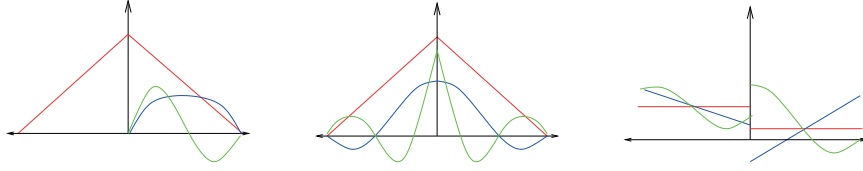


Figure 4.10: Examples of hierarchical bases spanning two 1D elements

scales going to $\overline{\mathbf{W}}$ and $\overline{\mathbf{U}}$ and the smaller scales to $\widetilde{\mathbf{W}}$ and $\widetilde{\mathbf{U}}$. We then make the following modelling assumptions for LES:

1. The unresolved scales have negligible influence on large scales. The large-scale equation then becomes:

$$B(\overline{\mathbf{W}}, \overline{\mathbf{U}}) + B'(\overline{\mathbf{W}}, \overline{\mathbf{U}}, \widetilde{\mathbf{U}}) - R(\overline{\mathbf{W}}, \widetilde{\mathbf{U}}) = (\overline{\mathbf{W}}, \mathbf{S}) \quad (4.72)$$

The motivation for this assumption is the observation that turbulent energy exchanges occur between like scales. This assumption should hold if the small resolved scale range is sufficiently large.

2. The effects of unresolved scales on small scales can be represented in a single dissipative model term, $\mathbf{M}(\widetilde{\mathbf{W}}, \widetilde{\mathbf{U}})$. The small-scale equation then becomes:

$$B(\widetilde{\mathbf{W}}, \overline{\mathbf{U}}) + B'(\widetilde{\mathbf{W}}, \overline{\mathbf{U}}, \widetilde{\mathbf{U}}) - R(\widetilde{\mathbf{W}}, \widetilde{\mathbf{U}}) = (\widetilde{\mathbf{W}}, \mathbf{S}) + \mathbf{M}(\widetilde{\mathbf{W}}, \widetilde{\mathbf{U}}) \quad (4.73)$$

For our example, we will employ a Smagorinsky-like model for \mathbf{M} :

$$\mathbf{M}(\mathbf{W}, \mathbf{U}) = (\mathbf{W}_{,i}, \mathbf{F}_i^m)_{Q_n} - (\mathbf{W}, (\mathbf{F}_i^m) n_i)_{P_n} \quad (4.74)$$

where the model flux \mathbf{F}_i^m is similar in character to the viscous flux, but using the Smagorinsky definition of the eddy viscosity:

$$\nu_t = (C_s \Delta)^2 |S'_{ij}| \quad (4.75)$$

where S'_{ij} is the strain-rate tensor of the small resolved scales. This model is referred to as small-small, since the eddy viscosity is computed in terms of small-scale gradients, and the model is applied only to the small scales. This is shown diagrammatically in figure 4.11. Note that to compute C_s , a procedure similar to that given in chapter 4 can be used, but now the integration only applies in the small-scale region of the cascade, i.e. the region between the cut-off wavenumber for the large resolved scales and the cut-off wavenumber for the small resolved scales. This generally results in larger values for C_s . A nice feature of three-scale implementations is that one can recover the DNS and traditional LES approaches by choosing either a zero small or a zero large scale range, respectively.

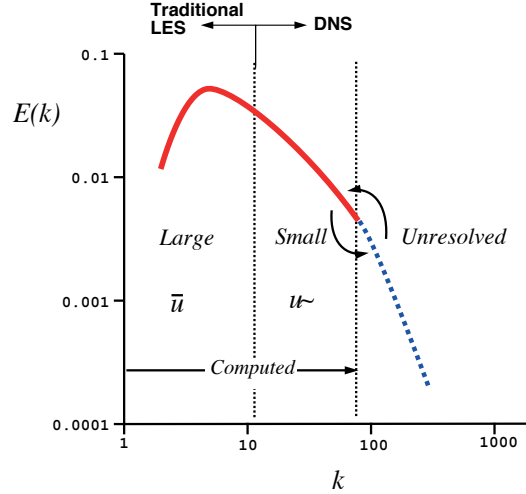


Figure 4.11: Model evaluation and application in three-scale VMM

The three-scale technique can also be interpreted as a two-scale method with a high-fidelity model for the unresolved scales. In this interpretation, the unresolved scales are $\tilde{\mathbf{U}}$, which we describe using modified Navier-Stokes equations (4.73) for a truncated version of \mathcal{V}'_n . In this interpretation the interaction terms in equation (4.72) are exact, and $\tilde{\mathbf{U}}$ will be zero when the exact solution is in $\bar{\mathcal{V}}_n$ and ν_t is computed with (4.75).

For the Smagorinsky LES results presented earlier in the chapter, the model, \mathbf{M} , was applied to all resolved scales. In the present context, this is equivalent to applying it in both the $\bar{\mathbf{W}}$ and $\tilde{\mathbf{W}}$ equations. This can have a negative effect on the fidelity of the largest of the resolved scales, resulting in an adverse impact on overall accuracy. Limiting the unresolved-scale model to the $\tilde{\mathbf{W}}$ equations can provide dramatic improvements, provided that the phenomena of interest is captured by the large resolved scales, $\bar{\mathbf{U}}$.

We now compare results for a turbulent channel flow in which the model is applied to all equations, and to only the $\tilde{\mathbf{W}}$ equations. A standard Smagorinsky model is used, but with a van Driest near-wall correction for eddy viscosity.

Using a numerically exact representation of the surface with a smooth initial condition will typically produce a laminar flow solution. To get the turbulent flow solution, an initial condition with turbulent-like perturbations is required. Since these will generally not correspond to the required turbulent condition, a transient develops, as shown in figure 4.12. The transient must be complete before statistics can be taken from the flow. For the case shown, this would be approximately after a time of 40. The period required for averaging can be significant, also on the order of 40 time units. Long averaging periods add to the expense, so moving window techniques can be used to estimate when

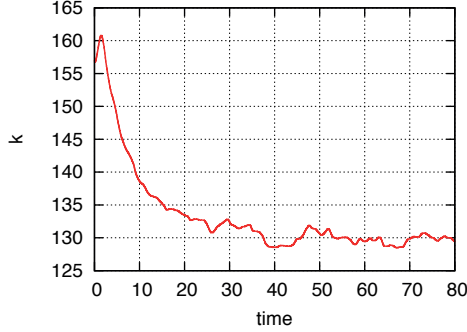


Figure 4.12: Kinetic energy time history for $Re_\tau = 180$ case

appropriate levels of error in the statistical quantities have been reached, in order to limit total run times.

In figure 4.13, a horizontal and vertical cutting plane are shown containing contours of velocity magnitude. Here the near-wall low-speed streaks can be seen, with dimensions roughly corresponding to those of the minimal flow unit.

We first examine a coarse-mesh computation using $8 \times 8 \times 8$ elements, each containing both linear and quadratic C^0 functions ($p = 2$) as a basis. Comparing with the minimal flow units, we note that the high-low variation between the streaks is just captured in by the small scale-space, which has a cut-off wavelength of $2 \times 720/(2 \times 8) = 90$ measured in plus units. Figure 4.14 shows the mean and root-mean-square fluctuating streamwise velocity profiles, computed with the traditional LES approach where the model is applied to all scales (SvD), and the three-scale approach where the model is applied only to the smallest of the resolved scales (VM). The VM results show some improvement over their single-scale counterparts, but agreement with the DNS is not yet satisfactory.

Now we consider a medium mesh of $16 \times 16 \times 16$ $p = 2$ elements. In this case the fundamental high-low variation of the streaks is captured in the large-scale space. For the three-scale method, this wavelength is therefore not directly influenced by the application of the Smagorinsky model. As shown in figure 4.15, the relative improvement is dramatic.

A similar effect can be seen when refining in p . Figure 4.16 shows results computed with $8 \times 8 \times 8$ $p = 3$ elements, which contain linear, quadratic and cubic interpolation polynomials. For the three-scale method the model is only applied to the equations describing the cubic variations. A similar level of improvement is observed as the fundamental streak variation is once again captured at wavelengths where the Smagorinsky model is not directly applied.²

²It is interesting to note that we have performed computations from the deterministic viewpoint, while employing a subgrid-scale model developed with a statistical viewpoint, and interpreted our results using a structural viewpoint

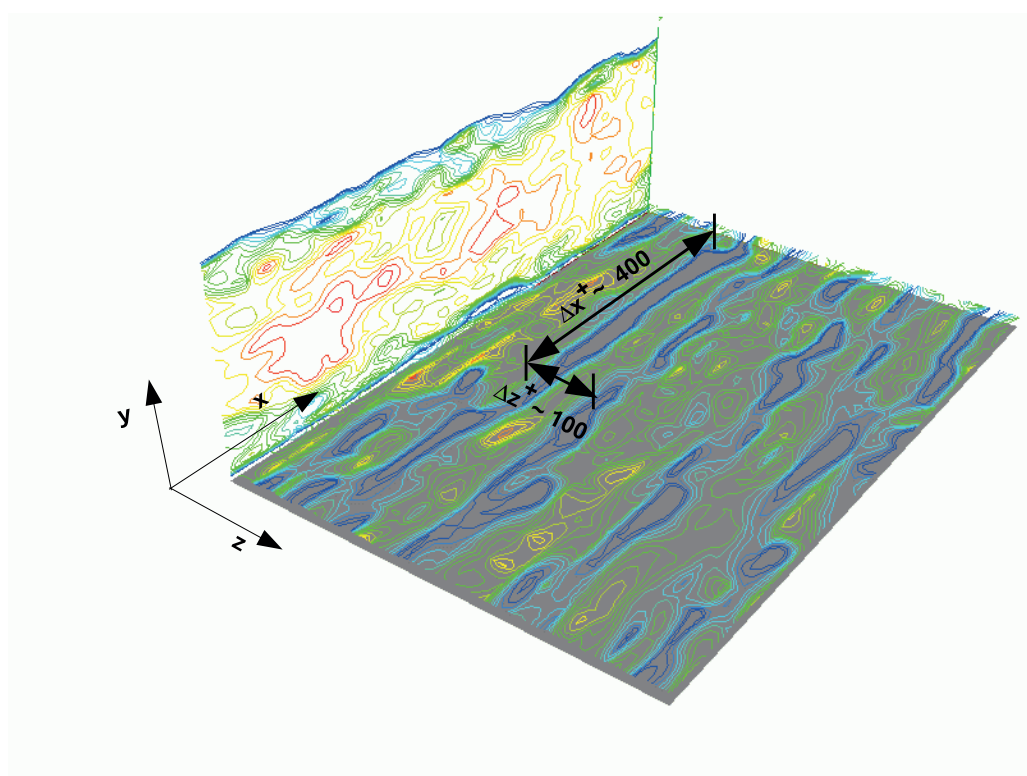


Figure 4.13: Velocity contours in a horizontal plane showing near-wall low-speed streaks

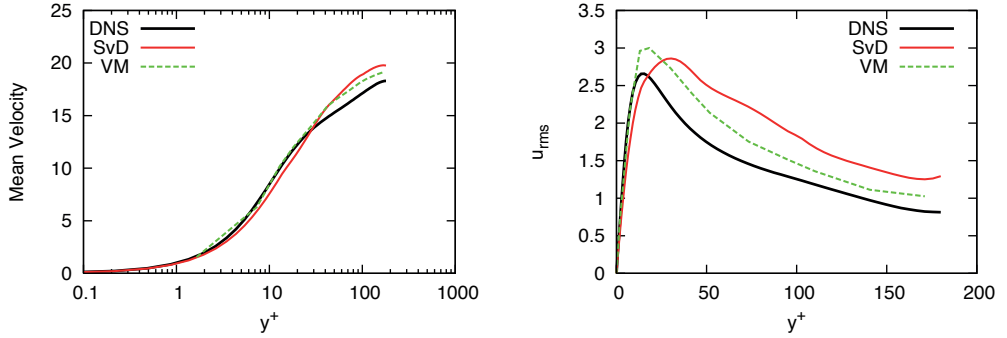


Figure 4.14: $Re_\tau = 180$ results computed with $8 \times 8 \times 8 p = 2$ elements

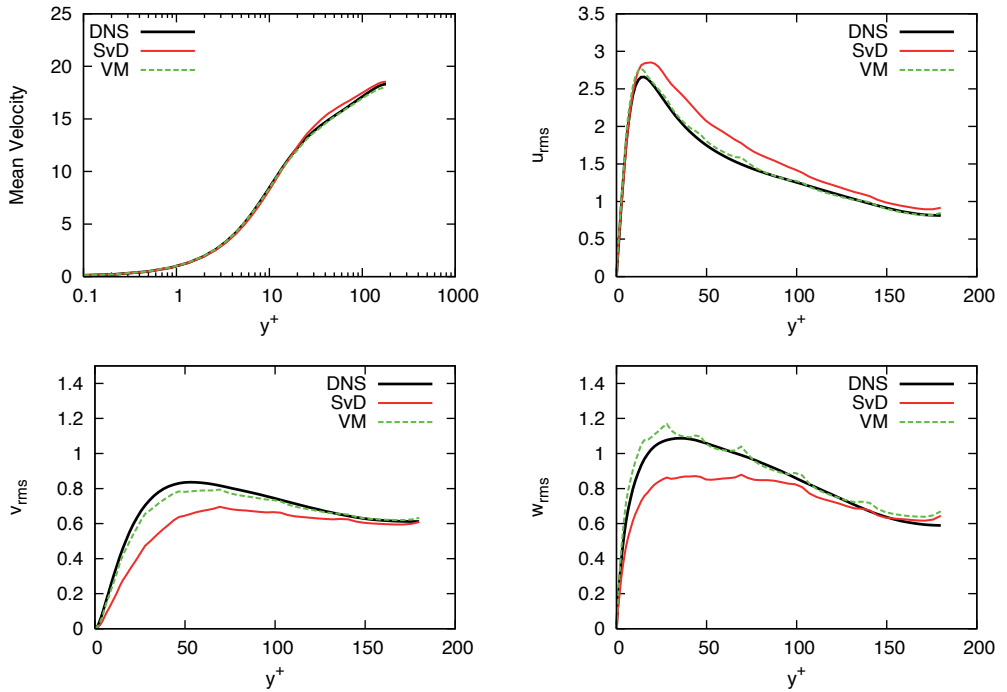


Figure 4.15: $Re_\tau = 180$ results computed with $16 \times 16 \times 16 p = 2$ elements

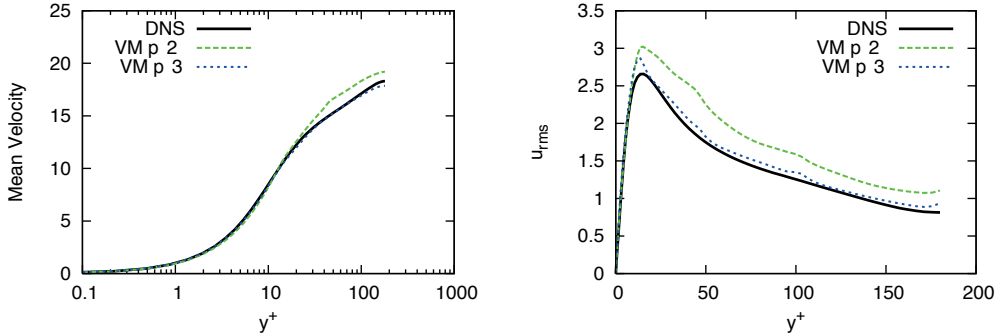


Figure 4.16: $Re_\tau = 180$ results computed with $8 \times 8 \times 8$ $p = 3$ elements

These results indicate that the accuracy of variational-multiscale methods is strongly rooted in their basic formulation, which preserves consistency with the Navier-Stokes equations at large scales, while providing realistic unresolved-scale interaction terms. The relative simplicity of the models in this and the previous section indicates there is some leeway in their design, provided that the projection of their effects onto $\overline{\mathbf{W}}$ is reasonable. This provides further avenues to explore in the approximation of unresolved-scale behaviour using combinations of algebraic, ordinary differential and partial differential equations. There thus remains much interesting research to be done in the determination of approximations which faithfully reproduce the essence of what we do not want to compute.

Chapter 5

RANS Methods

For engineering applications, the use of large-eddy simulations will not be routine for some time. This is because to obtain adequate statistics, large-eddy simulations require highly-resolved three-dimensional computations over extended simulation periods. If we give up the idea of (partly) computing turbulence, however, and propose to model all of it instead, the costs for considering realistic engineering problems drop dramatically. This is the motivation behind the use of Reynolds-averaged Navier-Stokes (RANS) methods, which employ complex empirical models to represent all the effects of turbulence on the mean flow. The computational requirement is thus reduced to a single steady-state computation per geometry, which may also be performed in two dimensions if the geometry under consideration is two-dimensional.

As RANS methods are relatively low in cost, they were the first to be widely applied. The first modern RANS turbulence models for computational fluid dynamics were developed in the early 1970s, followed by literally hundreds of others appearing through the 1980s and 1990s. This proliferation of models is an indication both of the importance of predicting the effects of turbulence, and of how difficult it is to develop a model which can be universally applied.

As descriptions for the basic phenomena governing turbulent flows remain under debate, RANS models must be developed with a combination of empiricism, dimensional analysis, consistency checks, experience and insight. In this chapter we will review the basic formulation of RANS methods, describe the design of the RANS models most commonly employed for aerospace applications.

5.1 Reynolds-averaged Navier-Stokes equations

Following Reynolds, we start by assuming a decomposition of the flow into the mean and fluctuating components:

$$u = \bar{u} + u' \quad (5.1)$$

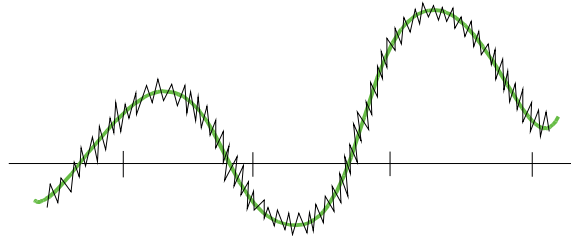


Figure 5.1: Slowly varying mean flow with rapid turbulent fluctuations

It is instructive to discuss what we mean by “mean” before deriving the corresponding equations of motion. One option for defining the mean flow is by the spatial average over a volume, V :

$$\bar{u}(t) = \lim_{V \rightarrow \infty} \frac{1}{V} \int \int \int u(x, t) dV \quad (5.2)$$

but this can only be applied in volumes where the turbulent fluctuations can be assumed to be isotropic, which is not the case for most engineering flows. Another option is the time average

$$\bar{u}(x) = \lim_{T \rightarrow \infty} \frac{1}{T} \int_t^{t+T} u(x, t) dt \quad (5.3)$$

which is well-defined for statistically steady turbulent flows, but becomes ambiguous when the boundary conditions of the problem vary in time. In such cases, there must be adequate time-scale separation between the changes in the boundary conditions and the unsteady fluctuations (figure 5.1). If general unsteady problems are considered, it is best to consider the mean flow to be the result of an ensemble average:

$$\bar{u}(x, t) = \lim_{N \rightarrow \infty} \frac{1}{N} \sum_N u(x, t) \quad (5.4)$$

The following identities hold for all the above definitions of the mean:

- $\bar{u}' = 0$
- $\overline{\bar{u}} = \bar{u}$
- $\overline{\bar{u}\bar{v}} = \bar{u}\bar{v}$
- $\overline{\bar{u}\bar{v}'} = 0$
- $\overline{\bar{u} + \bar{v}} = \bar{u} + \bar{v}$
- $\overline{\partial \bar{u} / \partial x} = \partial \bar{u} / \partial x$

The RANS equations can then be derived by substituting (5.1) into the incompressible Navier Stokes equations and then averaging the result, which gives:

$$\begin{aligned}\frac{\partial \bar{u}_i}{\partial x_i} &= 0 \\ \rho \frac{\partial \bar{u}_i}{\partial t} + \rho \frac{\partial}{\partial x_j} (\bar{u}_i \bar{u}_j) &= -\frac{\partial \bar{p}}{\partial x} + \frac{\partial}{\partial x_j} \left(\tau_{ij} - \rho \bar{u}'_i \bar{u}'_j \right)\end{aligned}\quad (5.5)$$

The above equations expresses the evolution of the mean solution. These are seen to be identical to the equations for the instantaneous velocity u , except the additional $-\rho \bar{u}'_i \bar{u}'_j$ arising from the nonlinear convective term. This additional term can be seen to act as an apparent stress, and is thus referred to as the *Reynolds stress tensor*. Note that it is not related to viscous processes in any way, but rather to the dynamics of the turbulent fluctuations (the majority of which are almost inviscid).

The behaviour of the Reynolds stress tensor must be specified in terms of the parameters of the problem and the unknown mean solution. This is called the *closure problem* of turbulence, and requires the introduction of an additional *turbulence model* to complete the solution for \bar{u}_i and \bar{p} . In these notes we will consider three basic approaches to constructing turbulence models. The first based on a linear eddy-viscosity assumption, the second based on non-linear eddy viscosities, and the last based on solving evolution equations for each of the Reynolds stress components. Before describing these approaches, we will consider the derivation of some additional useful relations from (5.5).

5.2 Additional dynamic relations

By taking moments of the Reynolds-averaged Navier-Stokes equations, it is possible to derive evolution equations for the Reynolds stress tensor and the turbulent kinetic energy, as described below.

5.2.1 The Reynolds-stress equations

Using continuity, we can write the incompressible momentum equation as:

$$NS(u_i) \equiv \rho \frac{\partial u_i}{\partial t} + \rho u_k \frac{\partial u_i}{\partial x_k} + \frac{\partial p}{\partial x} - \mu \frac{\partial^2 u_i}{\partial x_k \partial x_k} = 0 \quad (5.6)$$

Dynamic equations for the terms of the Reynolds stress tensor can then be derived by forming the following time average:

$$\overline{u'_i NS(u_j) + u'_j NS(u_i)} \quad (5.7)$$

After some manipulation the following is obtained (see [77]):

$$\begin{aligned}\frac{\partial \overline{u'_i u'_j}}{\partial t} + \bar{u}_k \frac{\partial \overline{u'_i u'_j}}{\partial x_k} &= \frac{\partial}{\partial x_k} \left(\nu \frac{\partial \overline{u'_i u'_j}}{\partial x_k} - \overline{u'_i u'_j u'_k} - \frac{\overline{p' u'_i}}{\rho} \delta_{jk} - \frac{\overline{p' u'_j}}{\rho} \delta_{ik} \right) \\ &\quad + \mathcal{P}_{ij} + \Phi_{ij} - \varepsilon_{ij}\end{aligned}\quad (5.8)$$

The terms on the left form the material derivative of the Reynolds stress components (divided by density), while the first term on the right represents their redistribution by viscous diffusion, turbulent transport, and pressure fluctuations. The remainder of the terms are the production tensor, given by:

$$\mathcal{P}_{ij} = -\overline{u'_i u'_k} \frac{\partial \bar{u}_j}{\partial x_k} - \overline{u'_j u'_k} \frac{\partial \bar{u}_i}{\partial x_k} \quad (5.9)$$

the pressure-strain correlation tensor:

$$\Phi_{ij} = \overline{\frac{p'}{\rho} \left(\frac{\partial u'_i}{\partial x_j} + \frac{\partial u'_j}{\partial x_i} \right)} \quad (5.10)$$

and the dissipation tensor:

$$\varepsilon_{ij} = 2\nu \overline{\frac{\partial u'_i}{\partial x_k} \frac{\partial u'_j}{\partial x_k}} \quad (5.11)$$

5.2.2 The turbulent kinetic energy equation

The turbulent kinetic energy is defined by:

$$k = \frac{1}{2} \left(\overline{u'^2} + \overline{v'^2} + \overline{w'^2} \right) = \frac{1}{2} \overline{u'_i u'_i} \quad (5.12)$$

A dynamic equation for k can therefore be derived by taking the trace of equation (5.8), resulting in:

$$\frac{\partial k}{\partial t} + \bar{u}_j \frac{\partial k}{\partial x_j} = \frac{\partial}{\partial x_j} \left(\nu \frac{\partial k}{\partial x_j} - \frac{\overline{p' u'_j}}{\rho} - \frac{\overline{u'_i u'_i u'_j}}{2} \right) + \mathcal{P} - \varepsilon \quad (5.13)$$

where in this case the production and dissipation (scalars) are defined by:

$$\mathcal{P} = -\overline{u'_i u'_j} \frac{\partial \bar{u}}{\partial x_j} \quad (5.14)$$

$$\varepsilon = \nu \overline{\frac{\partial u'_i}{\partial x_j} \frac{\partial u'_i}{\partial x_j}} \quad (5.15)$$

5.3 Linear eddy-viscosity models (LEVM)

We now return to the problem of modelling the Reynolds stress tensor, $-\rho \overline{u'_i u'_j}$. The first approach we consider is based on the Boussinesq approximation, where the Reynolds stress tensor is replaced by a linear combination of an effective eddy viscosity, μ_T , and the mean strain rate tensor, \bar{S}_{ij} :

$$-\rho \overline{u'_i u'_j} = 2\mu_T \bar{S}_{ij} \quad (5.16)$$

The Boussinesq approximation is by far the most popular approach to turbulence modelling in numerical simulations. When used, the turbulence model need only communicate with the rest of the Navier-Stokes code by providing a locally value for viscosity, which facilitates the simple switching between models. The Boussinesq approximation can also promote numerical stability due to the dissipative form of the approximation. In some linear eddy-viscosity models (LEVM), the turbulent kinetic energy, k , is predicted along with μ_T . In this case the following Boussinesq approximation is used:

$$-\rho \overline{u'_i u'_j} = 2\mu_T \bar{S}_{ij} - \frac{2}{3}\rho k \delta_{ij} \quad (5.17)$$

where the last term is added to ensure that the correct trace of the Reynolds stress tensor is obtained, since for incompressible flow $\bar{S}_{kk} = 0$.

There are a large number of different LEVM in use. The most complex of these solve one or more partial differential equations to determine μ_t . They have therefore been broken up into classes based on the number of partial differential equations to be solved. The most common instances of these classes are summarised below:

- **Zero-equation models:** One or more algebraic expressions, often based on mixing length theory, are used to predict the eddy viscosity.
- **Half-equation models:** Algebraic models for the eddy viscosity are combined with an additional ODE for describing the streamwise development of the maximum Reynolds shear stress.
- **One-equation models:** Models are provided for the uncomputable terms in (5.12), and the eddy viscosity is computed from the kinetic energy algebraically, or alternatively a PDE based on dimensional and empirical arguments is used to model the transport, production and dissipation of eddy viscosity directly.
- **Two-equation models:** Models are provided for the uncomputable terms in (5.12), and a PDE is introduced for the transport of an additional variable, normally dissipation or inverse time scale, based on dimensional and empirical arguments. The eddy viscosity is computed from the kinetic energy and the additional variable.

In the following section, we will first consider one of the most commonly used models in aerospace applications, and then discuss some of the limitations of LEVM in general.

5.3.1 An example LEVM: The Spalart-Allmaras model

A common approach to the RANS simulation of aerodynamic flows is to use a one-equation model based on a transport equation for the eddy viscosity. This

concept was first introduced by Nee and Kovasznay [47], and later refined by Baldwin and Barth [5] and Spalart and Allmaras [63]. The Spalart-Allmaras (SA) model and its variants have since become very popular, due to their competitive accuracy and relatively low cost [33, 8]. The transport equation for eddy viscosity was derived based on dimensional and empirical arguments, rather than by first principles. Its use offers a significant advantage over algebraic techniques, however, as it introduces the ability to model history effects due to flow convection. In analogy to the Reynolds stress equations, it has production and diffusion terms, although their design is motivated purely by modelling considerations.

The Spalart-Allmaras model does not produce an estimate for turbulent kinetic energy, so it is used with the Boussinesq assumption (5.16). A key aspect of the model is that the transport equation is not written for the eddy viscosity itself, but for an effective eddy viscosity $\tilde{\nu}$. This is scaled so that it varies linearly in the near-wall region, allowing its behaviour to be captured on relatively coarse meshes. The complete form of the model is :

$$\frac{\partial \tilde{\nu}}{\partial t} + \bar{u}_j \frac{\partial \tilde{\nu}}{\partial x_j} = c_{b1} \tilde{S} \tilde{\nu} - c_{w1} f_w \left(\frac{\tilde{\nu}}{d} \right)^2 + \frac{c_{b2}}{\sigma} \frac{\partial \tilde{\nu}}{\partial x_k} \frac{\partial \tilde{\nu}}{\partial x_k} + \frac{1}{\sigma} \frac{\partial}{\partial x_k} \left[(\nu + \tilde{\nu}) \frac{\partial \tilde{\nu}}{\partial x_k} \right] \quad (5.18)$$

where

$$\begin{aligned} \nu_t &= \tilde{\nu} f_{v1}, \quad \chi = \tilde{\nu}/\nu, \quad r = \frac{\tilde{\nu}}{\tilde{S} \kappa^2 d^2}, \quad g = r + c_{w2}(r^6 - r), \\ f_{v1} &= \frac{\chi^3}{\chi^3 + c_{v1}^3}, \quad f_{v2} = \frac{\chi}{1 + \chi f_{v1}}, \quad f_w = g \left[\frac{1 + c_{w3}^6}{g^6 + c_{w3}^6} \right], \\ \tilde{S} &= \sqrt{\Omega_{ij} \Omega_{ij}} + \frac{\tilde{\nu}}{\kappa^2 d^2} f_{v2}, \quad \Omega_{ij} = \left(\frac{\partial \bar{u}_i}{\partial x_j} - \frac{\partial \bar{u}_j}{\partial x_i} \right) \end{aligned} \quad (5.19)$$

here d is the distance from the wall, κ is the von Karman constant, and $c_{b1}, c_{w2}, \sigma, c_{w3}$ and c_{v1} are model constants. The terms on the right-hand side of (5.18) model production, destruction due to wall proximity, and conservative and non-conservative diffusion effects, respectively. As it was developed with wall-bounded flows in mind, the Spalart-Allmaras model does rather well in comparison with the channel DNS once sufficiently refined, as shown in figure 5.2. Note that for the results of the figure, uniform meshes are used. In most cases, the number of degrees of freedom required for accurate answers can be lowered by using mesh stretching to increase refinement near the wall.

Generally, the results obtained using the Spalart-Allmaras model for wall-bounded flows with mild pressure gradients can be quite good. Figure 5.3 shows results from the NASA CFL3D database for a NACA0012 airfoil at a zero angle of attack. With sufficient refinement, the predicted drag values match well with experiment. In more challenging situations, however, SA and other LEVM tend to have difficulties. Separated flows in particular can be difficult to compute

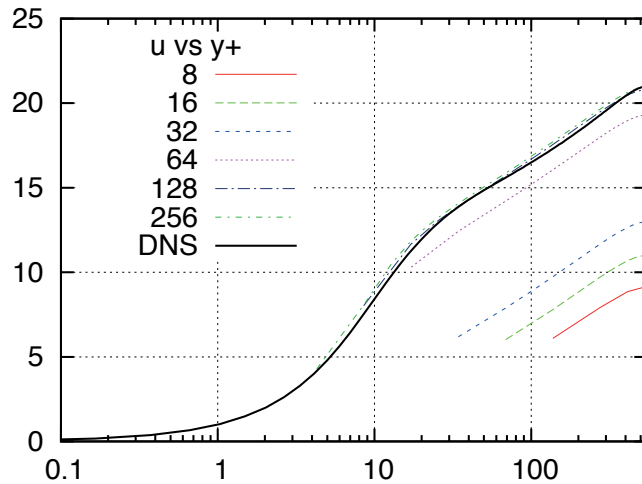


Figure 5.2: Mean velocity profile for turbulent channel flow computed with the Spalart-Allmaras model using a linear finite-element method for different numbers of wall-normal elements

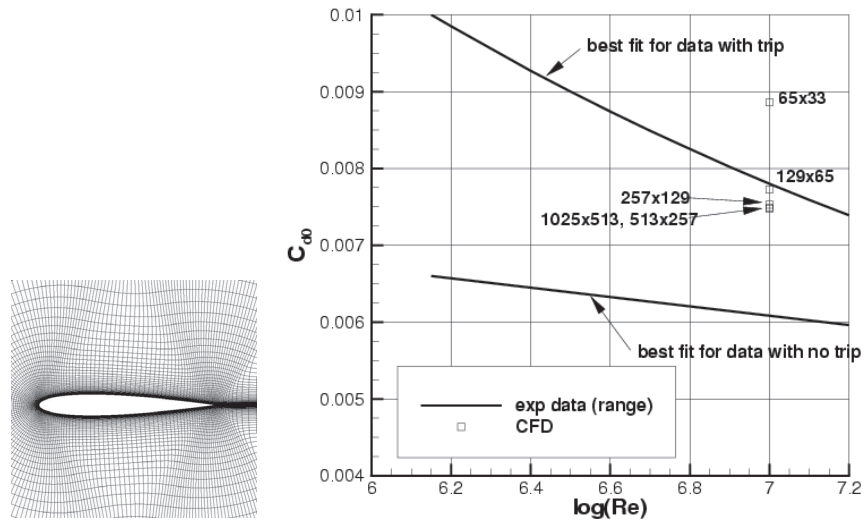


Figure 5.3: Example grid (left) and computed values of the drag coefficient compared with experiment (right) for a NACA 0012 airfoil at a zero angle of attack (from the NASA CFL3Dv6 test case database).

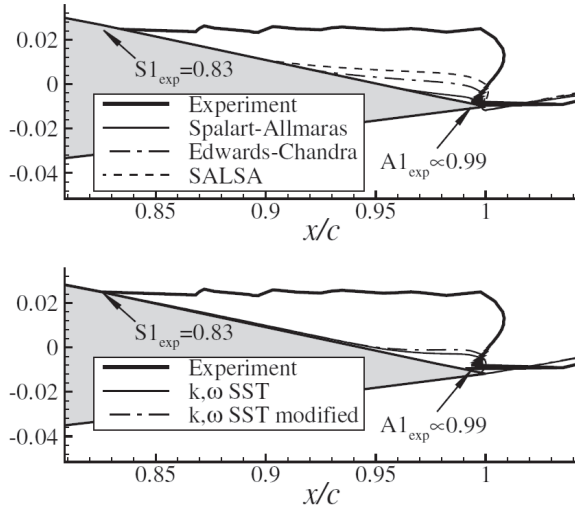


Figure 5.4: Experimental recirculation region at an airfoil trailing edge compared with RANS results using different turbulence models (from Celić and Hirschel [8])

accurately. Figure 5.4 shows the recirculation region near an airfoil trailing edge measured by experiment compared with predictions from various LEVM. Each model predicts the separation point too far aft in this case, which results in poor predictions of the extent of the recirculation. Limitations inherent to the LEVM approach will be discussed in the next section.

5.3.2 Limitations of LEVM

Representation of normal Reynolds stresses

A limitation of LEVM is their inability to properly represent the behaviour of the *normal* Reynolds stresses. This is most obviously demonstrated by considering parallel flow above a solid wall, where \bar{u} is only a function of y (figure 5.5). In this case, the estimates for all the normal Reynolds stresses components provided by (5.16) or (5.17) are identical, being either zero or $(2k/3)$. This is inappropriate since turbulent flow is highly anisotropic in the direction normal to the wall.

Since most LEVM are parameterised by wall normal distance, anisotropic effects above plane walls can be indirectly accounted for by other mechanisms in the model. In cases including curved, rotating or secondary flows, however, the magnitude of the changes to the normal Reynolds stresses are important, and some predictions of their values must be made. This is illustrated by example of [15], who considers a transition of a 2D parallel flow to a region of concave curvature as shown in figure 5.6. In this case, a re-distribution of turbulence pro-

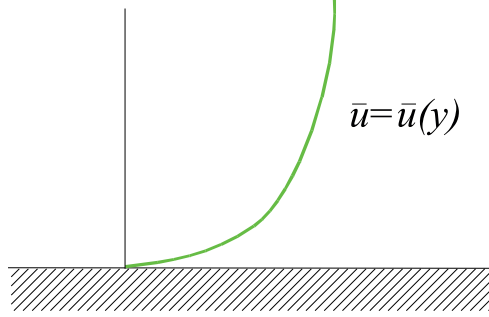


Figure 5.5: Parallel flow above a solid wall

duction among Reynolds-stress components will occur due to rotational strains.

For 2D flow, the production terms due to rotational strains $\left(\frac{\partial \bar{u}}{\partial y}, \frac{\partial \bar{v}}{\partial x}\right)$ are:

$$\mathcal{P}_{11} = -2\bar{u}'\bar{v}'\frac{\partial \bar{u}}{\partial y} \quad (\text{Production of } \overline{u'^2}) \quad (5.20)$$

$$\mathcal{P}_{21} = -\bar{u}^2\frac{\partial \bar{v}}{\partial x} - \bar{v}^2\frac{\partial \bar{u}}{\partial y} \quad (\text{Production of } \overline{u'v'}) \quad (5.21)$$

$$\mathcal{P}_{22} = -2\bar{u}'\bar{v}'\frac{\partial \bar{v}}{\partial x} \quad (\text{Production of } \overline{v'^2}) \quad (5.22)$$

Due to the no-slip condition, $\frac{\partial \bar{u}}{\partial y}$ will be large and positive, while $\frac{\partial \bar{v}}{\partial x}$ will be positive in the region of curvature. Also, $\overline{u'^2}$ tends to be much larger than $\overline{v'^2}$ in such flows. As the flow moves into the region of curvature, \mathcal{P}_{21} will become substantially more negative, meaning that the time rate of change of $\overline{u'v'}$ will be more negative. This will result in an increase in the magnitude of \mathcal{P}_{11} and \mathcal{P}_{22} , and correspondingly $\overline{u'^2}$ and $\overline{v'^2}$. Consequently, concave wall curvature tends to increase the intensity of turbulence, while convex wall curvature tends to reduce turbulence intensity. Since in LEVM we assume the Reynolds stresses are simply proportional to \bar{S}_{ij} , this kind of redistribution of production between components cannot be represented.

In [44] it was found that when the radius of curvature is 100 times the boundary layer thickness, skin friction can differ from its flat-wall value by up to 10%. Since curvature occurs in many flows of interest, there has been significant efforts to develop curvature corrections for LEVM so that they can still produce useful results in such situations [61].

Instantaneous dependence on \bar{S}_{ij}

A second limitation of LEVM is that they predict that the Reynolds stresses change instantaneously with the mean rate of strain. Experiments have demon-

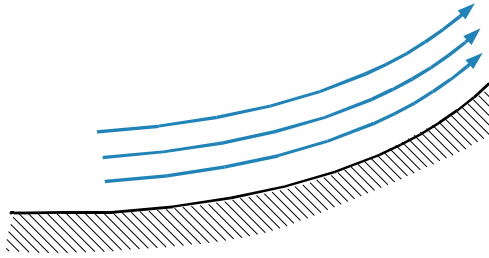


Figure 5.6: Curved streamlines over a concave wall

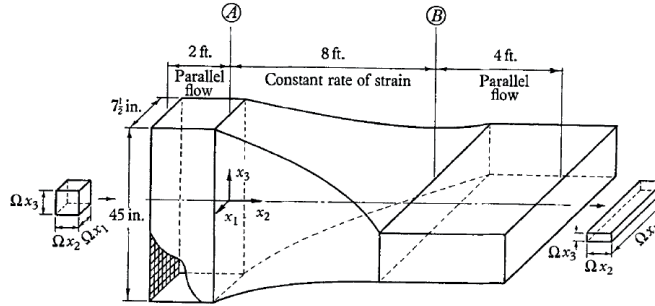


Figure 5.7: Geometry of the Tucker-Reynolds plane-strain flow experiment
(From Tucker and Reynolds [75])

strated, however, that in flows with sudden changes in the mean strain rate, the turbulence characteristics respond only gradually. An example is the transition from a flow of isotropic turbulence to one with nearly uniform mean strain and then back to zero mean strain described in [75, 77, 78] (figures 5.7 and 5.8). The result for a two-equation LEVM (dashed line) is seen to adjust suddenly to the removal of the strain rate while the experimental results (symbols) show a gradual return to an isotropic condition.

5.4 Non-linear constitutive relations (NLCR)

The representation of the normal Reynolds stress components can be improved by using more complex expressions to replace (5.16) and (5.17). Instead of being linear in the mean strain rate, for example, the expression of the Reynolds stresses can involve products of the mean strain and vorticity rate tensors:

$$\bar{S}_{ij} = \frac{1}{2} \left(\frac{\partial \bar{u}_i}{\partial x_j} + \frac{\partial \bar{u}_j}{\partial x_i} \right); \quad \bar{\Omega}_{ij} = \frac{1}{2} \left(\frac{\partial \bar{u}_i}{\partial x_j} - \frac{\partial \bar{u}_j}{\partial x_i} \right)$$

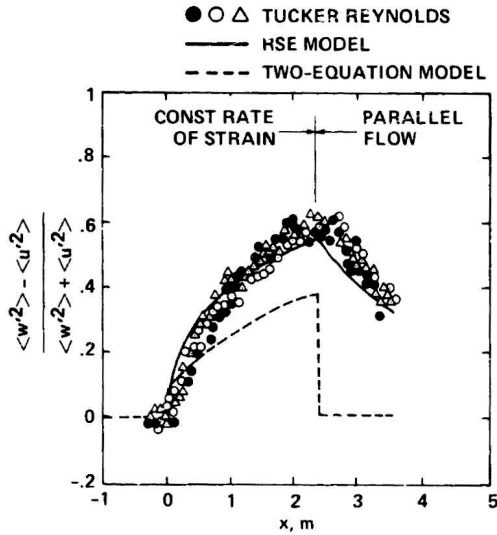


Figure 5.8: Computed and measured distortion parameter for the Tucker-Reynolds plane-strain flow (From Wilcox and Rubesin [78])

Such expressions are referred to as Non-linear constitutive relations (NLCR). An early example of a NLCR was introduced in 1970 by Lumley [40], which included quadratic terms in \bar{S}_{ij} and $\bar{\Omega}_{ij}$ based on an analogy with non-Newtonian flows. As described in the following sections, NLCR are usually constructed using dimensional arguments and mathematical constraints implied by the form of the Reynolds stress tensor, or by establishing a link with terms in the Reynolds-stress equations (5.8).

5.4.1 Non-linear eddy viscosity models (NLEVM)

In 1975 Pope [53] derived a general constitutive relation by considering the limits of expressing the Reynolds stresses in terms of polynomials of \bar{S}_{ij} and $\bar{\Omega}_{ij}$ imposed by the Cayley-Hamilton theorem¹. Models starting from this form and then proceeding to derive coefficients based on empirical arguments are normally referred to as anisotropic or non-linear eddy viscosity models (NLEVM). A recent example is the cubic form developed by Craft et al [14, 13] in which the

¹The Cayley-Hamilton states that a square matrix will satisfy its own characteristic polynomial (i.e. when the matrix is substituted in place of the eigenvalue into the characteristic polynomial).

Reynolds stresses are modelled as:

$$\begin{aligned}
 \overline{u'_i u'_j} &= \frac{2}{3} k \delta_{ij} - \nu_t \bar{S}_{ij} + c_1 \frac{\nu_t k}{\tilde{\varepsilon}} \left(\bar{S}_{ik} \bar{S}_{kj} - \frac{1}{3} \bar{S}_{kl} \bar{S}_{kl} \delta_{ij} \right) \\
 &\quad + c_2 \frac{\nu_t k}{\tilde{\varepsilon}} \left(\bar{\Omega}_{ik} \bar{S}_{kj} + \bar{\Omega}_{jk} \bar{S}_{ki} \right) + c_3 \frac{\nu_t k}{\tilde{\varepsilon}} \left(\bar{\Omega}_{ik} \bar{\Omega}_{jk} - \frac{1}{3} \bar{\Omega}_{lk} \bar{\Omega}_{lk} \delta_{ij} \right) \\
 &\quad + c_4 \frac{\nu_t k^2}{\tilde{\varepsilon}^2} \left(\bar{S}_{ki} \bar{\Omega}_{lj} + \bar{S}_{kj} \bar{\Omega}_{li} \right) \bar{S}_{kl} \\
 &\quad + c_5 \frac{\nu_t k^2}{\tilde{\varepsilon}^2} \left(\bar{\Omega}_{il} \bar{\Omega}_{lm} \bar{S}_{mj} + \bar{S}_{il} \bar{\Omega}_{lm} \bar{\Omega}_{mj} - \frac{2}{3} \bar{S}_{lm} \bar{\Omega}_{mn} \bar{\Omega}_{nl} \delta_{ij} \right) \\
 &\quad + c_6 \frac{\nu_t k^2}{\tilde{\varepsilon}^2} \bar{S}_{ij} \bar{S}_{kl} \bar{S}_{kl} + c_7 \frac{\nu_t k^2}{\tilde{\varepsilon}^2} \bar{S}_{ij} \bar{\Omega}_{kl} \bar{\Omega}_{kl}
 \end{aligned} \tag{5.23}$$

where k is the turbulent kinetic energy, $\tilde{\varepsilon}$ is the homogeneous dissipation rate, $\nu_t = c_\mu f_\mu k^2 / \tilde{\varepsilon}$ is a eddy viscosity corrected by nonlinear functions c_μ and f_μ and c_1, c_2, \dots, c_7 are model coefficients. Since \bar{S}_{ij} and $\bar{\Omega}_{ij}$ are computable from the main flow, all that is required to complete the expression is estimations for k and $\tilde{\varepsilon}$. These are provided by two modelled transport equations for k and $\tilde{\varepsilon}$, as is done in two-equation LEVM.

5.4.2 Algebraic Reynolds stress models (ARSM)

A second approach to obtaining NLCR models is to derive nonlinear algebraic relations directly from the Reynolds-stress transport equations (5.8). The classic example is due to Rodi [56], who assumed the anisotropy tensor a_{ij} :

$$a_{ij} = \frac{\overline{u'_i u'_j}}{k} - \frac{2}{3} \delta_{ij} \tag{5.24}$$

has a zero time derivative

$$\frac{\partial a_{ij}}{\partial t} = \frac{1}{k} \frac{\partial \overline{u'_i u'_j}}{\partial t} - \frac{\overline{u'_i u'_j}}{k^2} \frac{\partial k}{\partial t} = 0 \tag{5.25}$$

The Reynolds stress equations (5.8) can then be simplified to [16]:

$$\mathcal{P}_{ij} - \frac{2}{3} \delta_{ij} \mathcal{P} + \Phi_{ij} - (\mathcal{P} - \varepsilon) a_{ij} = 0 \tag{5.26}$$

where $\varepsilon = \varepsilon_{ii}/2$ is the total dissipation rate and $\mathcal{P} = \mathcal{P}_{ii}/2$. Given a model for Φ_{ij} , k , and ε , (5.26) provides implicit algebraic relations for $\overline{u'_i u'_j}$. The result is referred to as an algebraic stress model (ASM) or algebraic Reynolds stress model (ARSM).

Pope's analysis [53], also described an approach to obtaining an explicit relations for the Reynolds stress tensor in terms of \bar{S}_{ij} and $\bar{\Omega}_{ij}$ from the implicit model of Rodi. Taulbee [71] and Gatski and Speziale [17] derived more general NLCR models using this approach. In the case of Gatski and Speziale, these

were for three-dimensional turbulent flows in non-inertial frames. Due to the complexity of the necessary mathematics, they employed symbolic manipulation programs. A more recent example of this approach is presented in [76].

It is interesting to note that when an ARSM is used the production term:

$$\mathcal{P}_{ij} = -\overline{u'_i u'_k} \frac{\partial \bar{u}_j}{\partial x_k} - \overline{u'_j u'_k} \frac{\partial \bar{u}_i}{\partial x_k} \quad (5.27)$$

requires no further modelling. This means that the interchange in Reynolds stresses described in the LEVM curvature example can be directly represented.

5.4.3 Limitations of NLCR models

In general, NLCR models provide considerably more freedom for the modelling of normal Reynolds stresses than available in LEVM. Advanced NLCR models have produced good results for flows with curvature or rotation, at costs which are comparable to those of LEVM. NLCR models still respond instantaneously to changes in mean strain and vorticity, however, and therefore miss some of the dynamic responses of the Reynolds stress tensor. To model flows with rapid transients, it is commonly asserted that the complete Reynolds-stress transports relations are required. This approach is discussed in the next section.

5.5 Reynolds-stress transport (RST) models

The most general approach to closure in current use is to solve transport equations for each the Reynolds stress tensor components. This is known as *second-moment closure* (SMC) or Reynolds-stress transport (RST) modelling.²

Although (5.8) provides six additional transport equations for the unique six symmetric components of the Reynolds stress tensor, its redistribution, pressure-strain and dissipation terms introduce many more new unknowns which must be modelled. Like in ARSM, however, the turbulence production terms require no further modelling. RST models also have the additional advantage of exactly representing the convective terms, allowing them to be effective for highly transient flows.

5.5.1 Modelling of redistribution terms

The viscous diffusion part of the redistribution terms does not require modelling, but the remaining terms:

$$\overline{u'_i u'_j u'_k} + \frac{\overline{p' u'_i}}{\rho} \delta_{jk} + \frac{\overline{p' u'_j}}{\rho} \delta_{ik} \equiv C_{ijk} \quad (5.28)$$

²The term “moment” originates from the statistical definition for n^{th} -order products of the deviation from a value. In this case we are considering second-order products of deviations in velocity.

do. It is normally assumed that the pressure-diffusion terms are negligible when compared to $\overline{u'_i u'_j u'_k}$. The latter is normally modelled using an assumption of gradient transport [69] as:

$$C_{ijk} = -C_s \frac{k}{\varepsilon} \left(\overline{u'_i u'_m} \frac{\partial \overline{u'_j u'_k}}{\partial x_m} + \overline{u'_j u'_m} \frac{\partial \overline{u'_i u'_k}}{\partial x_m} + \overline{u'_k u'_m} \frac{\partial \overline{u'_i u'_j}}{\partial x_m} \right) \quad (5.29)$$

which was first obtained in [34].

5.5.2 Modelling of pressure-strain terms

Most models for the pressure-strain correlation tensor are based on assumptions of local homogeneity. Analytic solution for homogenous flows suggest the form [69]:

$$\Phi_{ij} = A_{ij} + M_{ijkl} \frac{\partial \bar{u}_k}{\partial x_l} \quad (5.30)$$

where the first term is referred to as the “slow part” and the second term as the “rapid part”. A simple but common model for the slow part is:

$$\Phi_{ij}^{slow} = -C_1 \varepsilon a_{ij} \quad (5.31)$$

which acts to reduce stresses as long as the anisotropy tensor a_{ij} , is not zero. For this reason it is called the “return to isotropy” model.

Modelling of the rapid part is often accomplished by assuming that the flow is close enough to isotropy that a Taylor-series expansion about a state of isotropy can be made. A common example is the Launder, Reece and Rodi model [34]:

$$\begin{aligned} \Phi_{ij}^{rapid} = & C_2 k \bar{S}_{ij} + C_3 k \left(a_{ik} \bar{S}_{jk} + a_{jk} \bar{S}_{ik} - \frac{2}{3} a_{mn} \bar{S}_{mn} \delta_{ij} \right) \\ & + C_4 k (a_{ik} \bar{\Omega}_{jk} + a_{jk} \bar{\Omega}_{ik}) \end{aligned} \quad (5.32)$$

For near-wall flows, the complete approximation for Φ_{ij} becomes

$$\Phi_{ij} = \Phi_{ij}^{slow} + \Phi_{ij}^{rapid} + \Phi_{ij}^{wall} \quad (5.33)$$

where the last term is added to account changes due to the “pressure reflection” of the wall (see, for example [20, 16]).

5.5.3 Modelling of the dissipation rate tensor

In high-Reynolds number flows, the Kolmogorov isotropy assumption is invoked so that

$$\varepsilon_{ij} \approx \frac{2}{3} \varepsilon \delta_{ij} \quad (5.34)$$

where ε is the dissipation rate of turbulent kinetic energy. ε is normally obtained by solution of a model transport equation of the form:

$$\begin{aligned} \frac{\partial \varepsilon}{\partial t} + \bar{u}_j \frac{\partial \varepsilon}{\partial x_j} &= -C_{\varepsilon 1} \frac{\varepsilon}{k} \overline{u'_i u'_j} \frac{\partial \bar{u}_i}{\partial x_j} - C_{\varepsilon 2} \frac{\varepsilon^2}{k} \\ &\quad + C_\varepsilon \frac{\partial}{\partial x_i} \left(\frac{k \overline{u'_i u'_j}}{\varepsilon} \frac{\partial \varepsilon}{\partial x_j} \right) + \nu \nabla^2 \varepsilon \end{aligned} \quad (5.35)$$

This equation is identical to that used in the $k - \epsilon$ LEVM, except that the turbulent diffusion term is anisotropic. Like the pressure-strain terms, corrections have also been developed for near-wall flows.

5.5.4 RST models in practice

The expense of RST models is high relative to LEVM and NLCR models, as a large number of additional PDEs must be solved, and the resulting discretisation tends to be numerically stiff. Furthermore, for certain classes of wall-bounded flows, advanced LEVM are still able to provide superior predictions to those of current RST models, as the development of the former has received much more attention. Yet in many situations, the use of even relatively primitive RST models is justified. In the Tucker-Reynolds flow (figure 5.8), for example, the RST model results (solid line, labelled RSE) are inherently superior, both in the representation of turbulent production and the return to isotropy. As increasing computing power facilitates the development and use of more complex methods, RST models are likely to become more sophisticated in the future, and to become increasingly attractive in situations where a refined LES is too expensive.

5.6 Wall functions

Even with appropriate stretching, a significant amount of resolution can be required to accurately resolve the high gradients of a turbulent boundary layer in the immediate vicinity of the wall. For second-order finite volume or difference codes, placing the first mesh point at $y^+ = 1$ or lower may be required (see figure 5.9). The resulting computational requirements can be substantial, particularly for three-dimensional high-Reynolds number problems.

On the other hand, it is known from experiment that for mild pressure gradients, the mean turbulent velocity profile in the immediate vicinity of a wall is nearly invariant when expressed in wall units. One approach to reducing computational effort is therefore to place the first grid point above the wall in the logarithmic region (above $y^+ \approx 30$), and use a classical law-of-the wall such as (2.21) to fix its mean solution. This is referred to as using a *wall function*. It saves computational effort by eliminating the large number of degrees of freedom required to accurately resolve the gradients below the intermediate layer, and by avoiding the numerical stiffness associated with highly-refined anisotropic meshes.

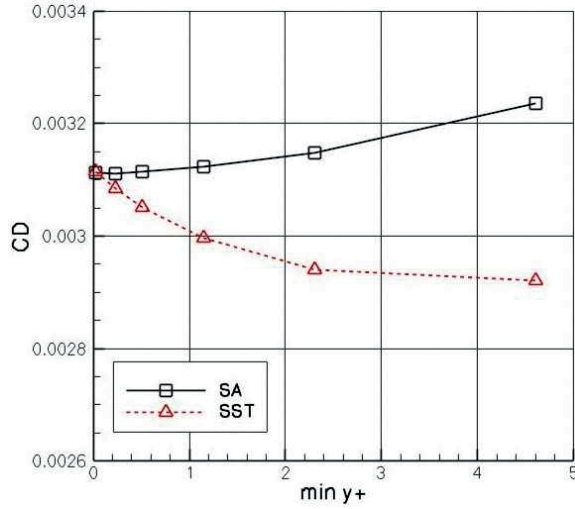


Figure 5.9: Effect of y^+ of first grid node on the the drag coefficient for a flat plate estimated with a second-order code and the Spalart-Allmaras and Menter SST turbulence models (from the NASA CFL3Dv6 test case database).

Using wall functions exactly in the way described above, however, leads to some difficulties. As the flow is generally unknown before the mesh is generated, it can be difficult to anticipate where the the first grid point should be placed so that it is contained within the logarithmic part of the profile. Secondly, the requirement that the first grid point be above $y^+ = 30$ makes it difficult to perform mesh refinement studies to verify grid independence, since the numerical error associated with a such a coarse near-wall mesh can be significant. These problems can be overcome by the use of *adaptive wall functions*, which automatically change the law used to predict the mean flow if the first grid point drops below $y^+ = 30$. An effective approach is to use a tabulated version of a well-refined near-wall profile obtained for a simpler case using the same turbulence model [29]. This ensures that consistent model parameters are available.

Chapter 6

Hybrid Methods

As described in the previous chapter, there exists a wide range of models which can be used for RANS computations. None of these, however, are able to robustly reproduce estimates for $-\rho\overline{u'_i u'_j}$ over the complete range of flows of interest to the engineer. The search for more sophisticated RANS models continues, but up to now there have been limits on the fidelity which can be achieved. Furthermore there are applications, such as aeroacoustics, where estimates of instantaneous fluctuations are desirable. Such information is not directly available from the RANS approach.

Consequently, in order to treat flows where a full LES is not yet practical, a number of hybrid procedures have been developed which use a combination of concepts from LES and RANS. In the following we will briefly discuss some issues involved in the design of hybrid methods, and describe the most commonly-used variant.

6.1 RANS, LES, URANS and Hybrids

The Reynolds-averaged Navier stokes equations (5.5) have obvious similarities with the previously-derived LES equations, but the way they are used is quite different. In RANS, \bar{u} is the mean velocity, and the turbulence model represents the effects of all fluctuations. Thus the solution for a steady flow can be obtained in a single time-independent computation. In LES, \bar{u} is the large-scale velocity which includes the largest of the turbulent fluctuations. To compute the mean, even for a steady problem, one must run a time-domain simulation until the largest turbulent scales fluctuate in a statistically stationary fashion, and then average the results of the simulation over a time interval long enough to establish the mean.

Things are a little less clear when one uses a program written for the RANS equations to perform a simulation which resolves the unsteady motion of large-scale vortical structures, an approach is known as URANS. When performed in two dimensions, the interpretation of URANS is difficult, as the large vortical

structures in the flow are incapable of engaging in the energy cascade, which is a fundamentally three-dimensional phenomena. When performed in three dimensions, on the other hand, URANS is essentially a form of LES, where the resolved-scale range is defined by the grid and solution interpolation, while the effect of the unresolved scales is represented by the RANS turbulence model. Standard RANS turbulence models, however, are not designed or calibrated for this purpose, and will not necessarily behave in a way which produces a compatible representation of unresolved-scale dynamics. In fact, experience has shown that a pure 3D URANS tends to impose excessive order and 2D behaviour on fundamentally 3D flows.

The interaction between RANS and LES is directly addressed in the design of hybrid methods. The biggest issue here is the incompatibility of the two flow representations. An LES region will require an estimation of instantaneous flow fluctuations on its boundaries, but this is not directly available from a RANS. If a zonal approach approach is used, where RANS and LES regions are clearly divided, then some procedure for generating synthetic fluctuations must be provided. This inevitably leads to a transition region between the synthetic fluctuations and those computed by the LES.

If a smooth blend between URANS and LES is used, then a transition region is still present, although harder to identify. As shown in [52], however, the resulting effects on the flow characteristics can be significant. The most popular hybrid method, DES, is based on a blended approach, and is described in the next section.

6.2 Detached Eddy Simulation (DES)

Detached Eddy Simulation (DES), was first introduced by Spalart [65, 68, 67] and has since seen wide application. The method is based on the Spalart-Allmaras LEVM described in section 5.3.1. The DES formulation consists simply of substituting the parameter \tilde{d} for d into (5.18) and (5.19), where

$$\tilde{d} = \min(d, C_{DES}\Delta) \quad (6.1)$$

where d is the distance from the wall, Δ is a length scale based on the largest dimension of the local grid cell, and C_{DES} has been calibrated based on experience to have a value near 0.65. Near the wall, when the aspect ration of the grid is high (large streamwise spacing) the model functions in “RANS mode”. If the streamwise resolution is increased however, the model switches locally to predict values of ν_T which are compatible with estimates for LES SGS models. Away from the wall, refined regions will operate in LES mode.

This approach does not always produce the desired mixture of RANS and LES. In particular as the streamwise grid spacing drops below the boundary layer thickness, the transition to LES can be abrupt. This issue has been addressed in a recent variant, delayed DES (DDES) [64], in which the RANS to LES transition is suppressed.

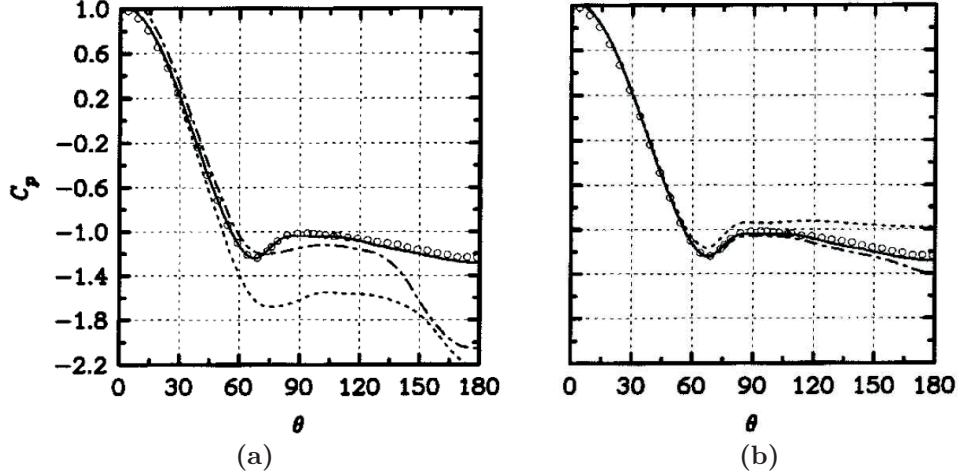


Figure 6.1: Pressure coefficient versus angular position for flow over a circular cylinder with $Re = 5 \times 10^4$. (a) Results from experiment (circles), 3D DES (solid line), 2D URANS (dashed line) and 2D DES (alternating short and long dashes). (b) Results from experiment (circles), coarse 3D DES (dashed line), medium 3D DES (solid line) and fine 3D DES (alternating short and long dashes). (From Travin et al (1999) [74])

Although simple in approach, DES has proven to provide a major quantitative improvements over 3D URANS. Results obtained for a circular cylinder appear in figures 6.1 (a) and (b). The first of these compares results from a 3D DES to those of a 2D URANS and a 2D DES, while the second puts the 3D DES results into perspective by indicating their still considerable grid dependence (note that the best answer is not provided by the fine grid). A qualitative comparison between RANS, 2D URANS, 3D URANS and DES appears in figure 6.2. This figure provides a clear illustration of the inherent differences between the formulations discussed in section 6.1.

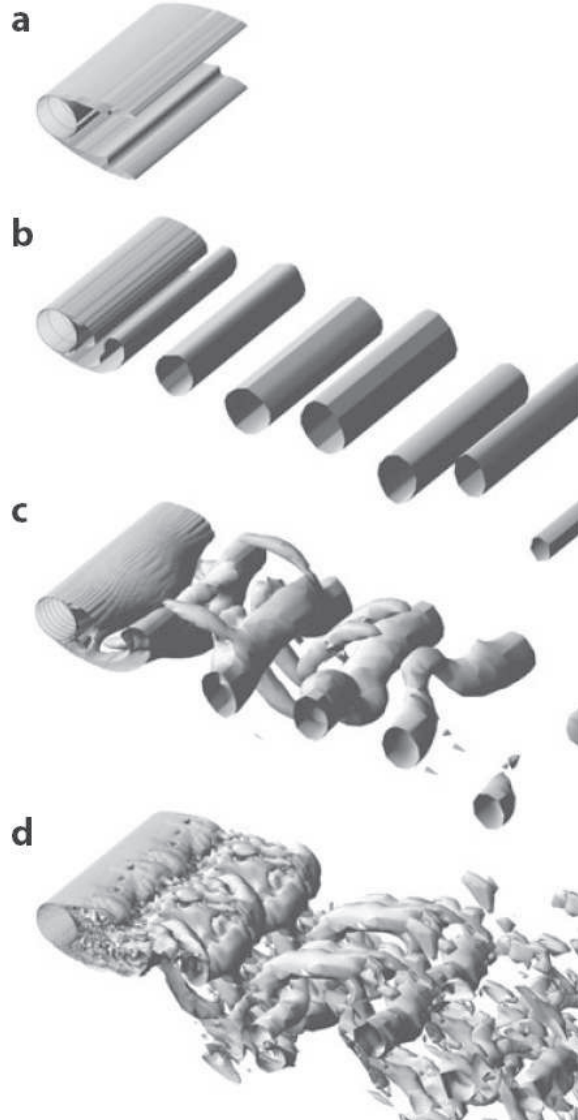


Figure 6.2: Vorticity isosurfaces near a circular cylinder, $Re_D = 5 \times 10^4$, Laminar separation. (a) RANS with SST model (b) 2D URANS, SA model, (c) 3D URANS, SA model, (d) DES with SA model (From Spalart (2009) [67])

Bibliography

- [1] *Isogeometric analysis of turbulence and fluid-structure interaction.*
- [2] Ronald J. Adrian. Closing in on models of wall turbulence. *Science*, 329(5988):155–156, 2010.
- [3] I. Akkerman, Y. Bazilevs, V.M. Calo, T.J. R. Hughes, and S. Hulshoff. The role of continuity in residual-based variational multiscale modeling of turbulence. *Computational Mechanics*, 41:371–378, 2008.
- [4] I. Akkerman, K.G. van der Zee, and S.J. Hulshoff. A variational germano approach for stabilized finite element methods. *Computer Methods in Applied Mechanics and Engineering*, 199(9-12):502 – 513, 2010.
- [5] B.S. Baldwin and T.J. Barth. A one-equation turbulence transport model for high Reynolds number wall-bounded flows. *NASA STI/Recon Technical Report N*, 91:10252, 1990.
- [6] Y. Bazilevs, V.M. Calo, J.A. Cottrell, T.J.R. Hughes, A. Reali, and G. Scovazzi. Variational multiscale residual-based turbulence modeling for large eddy simulation of incompressible flows. *Computer Methods in Applied Mechanics and Engineering*, 197(1-4):173–201, 2007.
- [7] P. S. Bernard and J. M. Wallace. *Turbulent Flow: Analysis, Measurement, and Prediction*. John Wiley and Sons, 2002.
- [8] A. Celić and E. Hirschel. Comparison of eddy-viscosity turbulence models in flows with adverse pressure gradient. *AIAA Journal*, 44(10):2156–2169, 2006.
- [9] G.T. Chapman and M. Tobak. Observations, theoretical ideas and modeling of turbulent flows – past, present and future. In Dwoyer et al., editor, *Theoretical Approaches to Turbulence*, Lecture Notes in Computational Science and Engineering, pages 19–49. Springer-Verlag, 1985.
- [10] Ramon Codina, Javier Principe, Oriol Guasch, and Santiago Badia. Time dependent subscales in the stabilized finite element approximation of incompressible flow problems. *Computer Methods in Applied Mechanics and Engineering*, 196(21):2413–2430, 2007.

- [11] S. S. Collis. The DG/VMS method for unified turbulence simulation. *AIAA Paper*, (2002-3124), 2002.
- [12] S. Corrsin. Outline of some topics in homogeneous turbulent flow. *J. Geophys. Res.*, 64(12):2134–2150, 1959.
- [13] T.J. Craft, H. Iacovides, and J.H. Yoon. Progress in the use of non-linear two-equation models in the computation of convective heat-transfer in impinging and separated flows. *Flow, Turbulence and Combustion*, 63:59–80, 2000.
- [14] TJ Craft, BE Launder, and K. Suga. Development and application of a cubic eddy-viscosity model of turbulence. *International Journal of Heat and Fluid Flow*, 17(2):108–115, 1996.
- [15] L. Davidson. An introduction to turbulence models. *Chalmers University Publication*, 97/2, 2003.
- [16] P. A. Durbin. *Turbulence Closure Models for Computational Fluid Dynamics*, chapter 10. Encyclopedia of Computational Mechanics. Wiley, 2004.
- [17] T. B. Gatski and C. G. Speziale. On explicit algebraic stress models for complex turbulent flows. *Journal of Fluid Mechanics*, 254:59–78, 1993.
- [18] M. Germano, U. Piomelli, P. Moin, and W. H. Cabot. A dynamic subgrid-scale eddy viscosity model. *Physics of Fluids A: Fluid Dynamics*, 3(7):1760–1765, 1991.
- [19] S. Ghosal, T. S. Lund, P. Moin, and K. Akselvoll. A dynamic localization model for large-eddy simulation of turbulent flows. *Journal of Fluid Mechanics*, 286:229–255, 1995.
- [20] M. M. Gibson and B. E. Launder. Ground effects on pressure fluctuations in the atmospheric boundary layer. *Journal of Fluid Mechanics Digital Archive*, 86(03):491–511, 1978.
- [21] F. F. Grinstein and C. Fureby. Monotonically Integrated Large Eddy Simulation of Free Shear Flows. *AIAA Journal*, 37(5):544–556, 1999.
- [22] TY Han, JCS Meng, and GE Innis. An open boundary condition for incompressible stratified flows. *Journal of Computational Physics*, 49:276–297, 1983.
- [23] S. Hoyas and Jiménez J. Scaling of the velocity fluctuations in turbulent channels up to $Re_\tau = 2003$. *Phys. Fluids*, 18, 2006.
- [24] T. J. R. Hughes, L. Mazzei, and K. E. Jansen. Large eddy simulation and the variational multiscale method. *Comput. Visual. Sci.*, (3):47–59, 2000.
- [25] Thomas JR Hughes, Guglielmo Scovazzi, and Leopoldo P Franca. Multi-scale and stabilized methods. *Encyclopedia of Computational Mechanics*.

- [26] N. Hutchins and I. Marusic. Large-scale influences in near-wall turbulence. *Philosophical Transactions of the Royal Society A: Mathematical, Physical and Engineering Sciences*, 365(1852):647, 2007.
- [27] J. Jiménez. *Turbulence and vortex dynamics*. Universidad Politècnica de Madrid, 2004.
- [28] J. Jimenez and P. Moin. The minimal flow unit in near-wall turbulence. *Journal of Fluid Mechanics*, 225(1):213–240, 1991.
- [29] G. Kalitzin, G. Medic, G. Iaccarino, and P. Durbin. Near-wall behavior of rans turbulence models and implications for wall functions. *Journal of Computational Physics*, 204(1):265 – 291, 2005.
- [30] M. Klein, A. Sadiki, and J. Janicka. A digital filter based generation of inflow data for spatially developing direct numerical or large eddy simulations. *Journal of Computational Physics*, 186(2):652–665, 2003.
- [31] A. N. Kolmogorov. Energy dissipation in locally isotropic turbulence. *Dokl Akad Nauk SSR*, 32:19–21, 1941.
- [32] A. N. Kolmogorov. Local structure of turbulence in an incompressible fluid at very high reynolds numbers. *Dokl Akad Nauk SSR*, 30:200–303, 1941.
- [33] L. D. Kral. Recent experience with different turbulence models applied to the calculation of flow over aircraft components. *Progress in Aerospace Sciences*, 34:481–541, 1998.
- [34] B. E. Launder, G. J. Reece, and W. Rodi. Progress in the development of a reynolds-stress turbulence closure. *Journal of Fluid Mechanics Digital Archive*, 68(03):537–566, 1975.
- [35] M. Lee and R. D. Moser. Direct numerical simulation of turbulent channel flow up to $re\tau = 5200$. *J. Fluid Mech.*, submitted, 2015.
- [36] M. Lee and R. D. Moser. Petascale direct numerical simulation of turbulent channel flow on up to 786k cores. *Physics of Fluids*, submitted, 2015.
- [37] D. K. Lilly. *The representation of small-scale turbulence in numerical simulation experiments*. Proc. IBM Scientific computing Symposium on Env. Sci. 1967.
- [38] K. Liu and R.H. Pletcher. Inflow conditions for the large eddy simulation of turbulent boundary layers: a dynamic recycling procedure. *Journal of Computational Physics*, 219(1):1–6, 2006.
- [39] E. N. Lorenz. Deterministic nonperiodic flow. *J. Atmos. Sci.*, 20:130–141, 1963.
- [40] J. L. Lumley. Toward a turbulent constitutive relation. *Journal of Fluid Mechanics Digital Archive*, 41(02):413–434, 1970.

- [41] T.S. Lund, X. Wu, and K.D. Squires. Generation of turbulent inflow data for spatially-developing boundary layer simulations. *Journal of Computational Physics*, 140(2):233–258, 1998.
- [42] I. Marusic, R. Mathis, and N. Hutchins. Predictive model for wall-bounded turbulent flow. *Science*, 329(5988):193–196, 2010.
- [43] J. M. McDonough. *Introductory lectures on Turbulence; Physics, Mathematics and Modeling*. University of Kentucky, 2007.
- [44] R. N. Meroney and P. Bradshaw. Turbulent boundary-layer growth over a longitudinally curved surface. *AIAA*, 13(11):1448–1453, 1975.
- [45] P. Moin and K. Mahesh. Direct numerical simulation: A tool in turbulence research. *Annual Review of Fluid Mechanics*, 30(1):539–578, 1998.
- [46] E. A. Munts, S. J. Hulshoff, and R. de Borst. A modal-based multi-scale method for large eddy simulation. *Journal of computational physics*, 224(1):389–402, 2002.
- [47] V.W. Nee and L.S.G. Kovasznay. Simple phenomenological theory of turbulent shear flows. *Physics of Fluids*, 12:473, 1969.
- [48] F. Nicoud, J. S. Baggett, P. Moin, and W. Cabot. Large eddy simulation wall-modeling based on suboptimal control theory and linear stochastic estimation. *Phys. Fluids*, 13, 2001.
- [49] S. A. Orszag and G. S. Patterson. Numerical simulation of turbulence: statistical models and turbulence. *Lecture notes in physics*, 12:127–147, 1972.
- [50] U. Piomelli. Large-eddy simulation: achievements and challenges. *Progress in Aerospace Sciences*, 35:335–362, 1999.
- [51] U. Piomelli. Wall-layer models for large-eddy simulations. *Progress in Aerospace Sciences*, 44(6):437 – 446, 2008.
- [52] U. Piomelli, E. Balaras, H. Pasinato, K.D. Squires, and P.R. Spalart. The inner-outer layer interface in large-eddy simulations with wall-layer models. *Int. J. of Heat and Fluid Flow*, 24:538–550, 2003.
- [53] S. B. Pope. A more general effective-viscosity hypothesis. *Journal of Fluid Mechanics*, 72(02):331–340, 1975.
- [54] S. B. Pope. Ten questions concerning the large-eddy simulation of turbulent flows. *New Journal of Physics*, 6(1):35, 2004.
- [55] Javier Principe, Ramon Codina, and Florian Henke. The dissipative structure of variational multiscale methods for incompressible flows. *Computer Methods in Applied Mechanics and Engineering*, 199(13):791–801, 2010.

- [56] W. Rodi. A new algebraic relation for calculating the Reynolds stresses. *Gesellschaft Angewandte Mathematik und Mechanik*, 56:219–, March 1976.
- [57] C. L. Rumsey, S. M. Rivers, and J. H. Morrison. Study of CFD variation on transport configurations from the second drag-prediction workshop. *Computers and Fluids*, 34(1):785–816, 2005.
- [58] P. Sagaut and C. Meneveau. *Large Eddy Simulation for Incompressible Flows: An Introduction*. Springer, 2006.
- [59] U. Schumann. Subgrid scale model for finite difference simulations of turbulent flow s in plane channels and annuli. *J. Comp. Physics*, 18:376–404, 1975.
- [60] J. Smagorinsky. General circulation experiments with the primitive equations. *Mon. Wea. Rev.*, 91:99164, 1963.
- [61] P. E. Smirnov and F. R Menter. Sensitization of the SST turbulence model to rotation and curvature by applying the spalart–shur correction term. *Journal of Turbomachinery*, 131(4):041010, 2009.
- [62] A. J. Smits, B. J. McKeon, and I. Marusic. Highreynolds number wall turbulence.
- [63] P. R. Spalart and S. R. Allmaras. A one-equation turbulence model for aerodynamic flows. *AIAA Paper*, (92-0439), 1992.
- [64] P. R. Spalart, S. Deck, M. L. Schur, K. D. Squires, M. K. Strelets, and A. Travin. A new version of detached-eddy simulation, resistant to ambiguous grid densities. *Theoretical and Computational Fluid Dynamics*, 20:181–195, 2006.
- [65] P. R. Spalart, W. H. Jou, M. Stretlets, and S. R. Allmaras. Comments on the feasibility of LES for wings and on the hybrid RANS/LES approach. In *Advances in DNS/LES: proceedings of the First AFOSR International Conference on DNS/LES, Louisiana Tech University, Ruston, Louisiana, August 4-8, 1997*, page 137. Greyden Press, 1997.
- [66] P.R. Spalart. Direct simulation of a turbulent boundary layer up to $R_\theta = 1410$. *Journal of Fluid Mechanics*, 187:61–98, 1988.
- [67] P.R. Spalart. Detached-eddy simulation. *Annual Review of Fluid Mechanics*, 41:181–202, 2009.
- [68] R. Spalart, P. Young Person’s Guide to Detached-Eddy Simulation Grids. Technical Report CR 2001-211032, NASA, July 2001.
- [69] C. G. Speziale, S. Sarkar, and T. B. Gatski. Modelling the pressure-strain correlation of turbulence: an invariant dynamical systems approach. *Journal of Fluid Mechanics*, 227:245–272, 1991.

- [70] C.K.W. Tam and J.C. Webb. Dispersion-relation-preserving finite difference schemes for computational acoustics. *J. Comput. Phys.*, 107(2):262–281, 1993.
- [71] D.B. Taulbee. An improved algebraic Reynolds stress model and corresponding nonlinear stress model. *Physics of Fluids A: Fluid Dynamics*, 4:2555, 1992.
- [72] H. Tennekes and J. L. Lumley. *A first course in turbulence*. MIT Press, 1972.
- [73] A. Tisnober. *An informal introduction to turbulence*. Fluid Mechanics and its applications. Kluwer, 2001.
- [74] A. Travin, M. Shur, M. L. Strelets, and P. R. Spalart. Detached-eddy simulations past a circular cylinder. *Flow, Turbulence and Combustion*, 63:293–313, 1999.
- [75] H. J. Tucker and A. J. Reynolds. The distortion of turbulence by irrotational plane strain. *Journal of Fluid Mechanics*, 32(04):657–673, 1968.
- [76] S. Wallin and A. V. Johansson. An explicit algebraic Reynolds stress model for incompressible and compressible turbulent flows. *Journal of Fluid Mechanics*, 403:89–132, 2000.
- [77] D. C. Wilcox. *Turbulence Modeling for CFD*. DCW Industries, Inc. La Cañada, California, 1994.
- [78] DC Wilcox and MW Rubesin. Progress in turbulence modeling for complex flow fields including effects of compressibility. *NASA STI/Recon Technical Report*, TP-1517(80-20527), 1980.
- [79] M. V. Zagarola. *Mean Flow Scaling of Turbulent Pipe Flow*. Ph.D. Thesis, Dep. of Mechanical and Aerospace Engineering. Princeton University, June 1996.

Appendix A

The Navier-Stokes equations

A.1 The incompressible Navier-Stokes Equations (NSE)

The equations of mass and momentum conservation for an incompressible Newtonian viscous flow are:

$$\begin{aligned}\frac{\partial u_i}{\partial x_i} &= 0 \\ \rho \frac{\partial u_i}{\partial t} + \rho \frac{\partial}{\partial x_j} (u_i u_j) &= - \frac{\partial p}{\partial x_i} + \frac{\partial \tau_{ij}}{\partial x_j}\end{aligned}\quad (\text{A.1})$$

where u_i is the velocity vector, p is the pressure, ρ is the density and τ_{ij} is the viscous stress tensor defined by:

$$\tau_{ij} = 2\mu S_{ij} \quad (\text{A.2})$$

where μ is the molecular viscosity and S_{ij} is the strain-rate tensor defined by:

$$S_{ij} = \frac{1}{2} \left(\frac{\partial u_i}{\partial x_j} + \frac{\partial u_j}{\partial x_i} \right) \quad (\text{A.3})$$

A.2 The equation for pressure

Taking the divergence of the incompressible NSE one has:

$$\frac{\partial^2 u_i}{\partial x_i \partial t} + \frac{\partial^2}{\partial x_i \partial x_j} \left(u_i u_j - u_i \frac{\partial u_j}{\partial x_j} \right) = - \frac{1}{\rho} \frac{\partial^2 p}{\partial x_i \partial x_i} + \nu \left(\frac{\partial}{\partial x_i} \frac{\partial^2 u_i}{\partial x_j \partial x_j} \right) \quad (\text{A.4})$$

Since $\frac{\partial u_i}{\partial x_i} = 0$, the first, third and last terms are zero, so we are left with:

$$\nabla^2 p = -\rho \frac{\partial^2 u_i u_j}{\partial x_i \partial x_j} \quad (\text{A.5})$$

A.3 The equation for vorticity

In vector notation, the incompressible momentum equation is:

$$\frac{\partial \mathbf{u}}{\partial t} + \mathbf{u} \cdot \nabla \mathbf{u} = -\frac{1}{\rho} \nabla p + \nu \nabla^2 \mathbf{u} \quad (\text{A.6})$$

To derive the vorticity equation, we take the curl of the above while noting that $\nabla \times \nabla p = 0$ and $\nabla \times (\nabla^2 \mathbf{u}) = \nabla^2(\nabla \times \mathbf{u})$:

$$\frac{\partial(\nabla \times \mathbf{u})}{\partial t} + \nabla \times (\mathbf{u} \cdot \nabla \mathbf{u}) = \nu \nabla^2(\nabla \times \mathbf{u}) \quad (\text{A.7})$$

Using the vector identity:

$$\nabla \times (\mathbf{u} \cdot \nabla \mathbf{u}) = \mathbf{u} \cdot \nabla(\nabla \times \mathbf{u}) - (\nabla \times \mathbf{u}) \cdot \nabla \mathbf{u} + (\nabla \cdot \mathbf{u})(\nabla \times \mathbf{u}) \quad (\text{A.8})$$

and noting that for an incompressible flow $\nabla \cdot \mathbf{u} = 0$, (A.7) becomes:

$$\frac{\partial(\nabla \times \mathbf{u})}{\partial t} + \mathbf{u} \cdot \nabla(\nabla \times \mathbf{u}) - (\nabla \times \mathbf{u}) \cdot \nabla \mathbf{u} = \nu \nabla^2(\nabla \times \mathbf{u}) \quad (\text{A.9})$$

or, defining the vorticity vector $\boldsymbol{\omega}$ as $\nabla \times \mathbf{u}$:

$$\frac{\partial \boldsymbol{\omega}}{\partial t} + \mathbf{u} \cdot \nabla \boldsymbol{\omega} = \boldsymbol{\omega} \cdot \nabla \mathbf{u} + \nu \nabla^2 \boldsymbol{\omega} \quad (\text{A.10})$$

Note that vorticity is not necessarily conserved, owing to the presence of both inviscid and viscous terms on the right hand side of the equation. The pressure field does not effect the vorticity, however, since its gradient acts as a local body force and therefore cannot induce the rotation of a fluid element.

The inviscid term on the right-hand side can be conveniently expressed in terms of the strain-rate, \mathbf{S} , by noting that for any vector \mathbf{b} :

$$\mathbf{b} \cdot \nabla \mathbf{u} = \mathbf{S} \cdot \mathbf{b} + \frac{1}{2}(\boldsymbol{\omega} \times \mathbf{b}) \quad (\text{A.11})$$

since $\boldsymbol{\omega} \times \boldsymbol{\omega} = 0$ we have finally:

$$\frac{\partial \boldsymbol{\omega}}{\partial t} + \mathbf{u} \cdot \nabla \boldsymbol{\omega} = \mathbf{S} \cdot \boldsymbol{\omega} + \nu \nabla^2 \boldsymbol{\omega} \quad (\text{A.12})$$